University of Dundee

Effect of soil deformability on the failure mechanism of shallow plate or screw anchors in sand

Cerfontaine, Benjamin; Knappett, Jonathan; Brown, Michael; Bradsaw, Aaron S.

Title: Effect of soil deformability on the failure mechanism of shallow plate or screw anchors in sand

Article Type: Research Paper

Corresponding Author: Mr. Benjamin Cerfontaine, PhD

Corresponding Author's Institution: University of Dundee

First Author: Benjamin Cerfontaine, PhD

Order of Authors: Benjamin Cerfontaine, PhD; Jonathan A Kappett, MA,MEng, PhD; Michael J Brown, BEng, PhD; Aaron S Bradshaw, PhD

Abstract: Most analytical approaches for the design of shallow plate and screw anchors in tension are based on the limit equilibrium of a rigid soil wedge for which a horizontal stress distribution acting on the failure plane is assumed.
Finite element analysis for a wide range of soil properties was carried out to identify the shape of the failure mechanism and to study the stress distribution at failure. Results show that soil deformation modifies the stress field around the anchor and increases the uplift capacity. A semi-analytical approach is proposed to describe this stress distribution, based on peak friction angle.

Effect of soil deformability on the failure mechanism of shallow plate or screw anchors in sand

1. Introduction

Installed offshore renewable energy output has increased exponentially throughout the world and particularly in Europe with 15.78GW of total installed capacity in 2017, mainly in the North Sea (Wind Europe 2018). Monopile foundations are dominant and represent 87% of the installed wind turbine substructures. However, these foundations are cost-effective only in relatively shallow water, close to shore (Wind Europe 2018). Deeper water, far from the coast, has a larger wind resource potential, a lower visual impact and represents most of the available locations for future wind turbines (European Wind Energy Association 2013). Such locations will require a move away from conventional fixed foundations towards anchored floating systems for instance. The anchors for such systems must be developed to decrease the overall costs and ensure economic viability of future wind farms, where foundations may represent up to 30% of current capital costs, while also being upscaled to support increasingly larger wind turbines.

Plate anchors and screw piles work in a similar way under tension loads. Plate anchors can be installed dynamically (e.g. O'Loughlin et al. 2014) or using suction caissons (Randolph et al. 2011). Their offshore dimensions are expected to reach several meters (O'Loughlin et al. 2014). Screw piles are mostly used onshore as foundations for light structures (Perko 2009). Their onshore dimensions typically range between 64-200mm for the core diameter and 150-400mm for the helix diameter. However, they have attracted greater attention recently as a possible foundation solution for offshore structures (Byrne and Houlsby 2015, Gaudin et al. 2017). Their behaviour under coupled lateral and compression loading was previously studied by Al-Baghdadi et al. (2015, 2017) and there is ongoing work to improve prediction of installation requirements (Al-Baghdadi et al. 2017b, Davidson et al. 2018). The use of screw piles as anchors has the potential to combine the uplift capacity of a plate anchor with the lateral resistance of a pile, coupled with the advantage of low-vibration/low-environmental impact during installation when compared to driven piles.

The uplift capacity of plate anchors and screw piles in sands has been investigated for several decades. Most experiments consist of 1g small-scale tests whose plate diameter was smaller than 100mm, as reported in Murray and Geddes (1987), Ghaly et al. (1991). Only a few centrifuge (Dickin 1988, Schiavon et al. 2016, Perez et al. 2017) and field (Tucker 1987, Tappenden 2007, Gavin et al. 2014) tests are available to compare results at larger scale. More recently detailed analysis has been undertaken using limit analysis of plate anchors as reported in Merifield et al. (2003), Merifield and Sloan (2006), and with Finite Element analysis (FEA) by Perez et al. (2017) for screw piles.

From a theoretical perspective, plate and screw anchors have been idealised similarly. The anchor uplift capacity is derived from the equilibrium of a rigid soil body delineated by a given failure surface. At shallow depths, the failure surface is a soil wedge reaching the surface, whose boundary may be assumed to be a straight line, either vertical or inclined, (Meyerhof and Adams 1968, Ghaly et al. 1991, Giampa et al. 2017) or a log-spiral (Murray and Geddes 1987, Saeedy 1987, Hanna et al. 2007) propagating from the plate to the soil surface (Figure 1Figure 1). At greater depths, a flow around mechanism has been proposed,

1

consisting of a deep wedge that does not reach the ground surface (Meyerhof and Adams 1968, Ghaly et al. 1991).

Several analytical approaches depending on the soil properties and geometry have been previously derived based on these analyses. At shallow embedment, the uplift capacity is typically obtained by considering the force equilibrium of a rigid wedge. However, there is no general agreement on the failure mechanism geometry (e.g. angle of wedge slip planes to the vertical), the depth at which transition occurs between shallow and deep modes of failure or the stress distribution that should be considered at failure. Most approaches include an empirical factor calibrated against small-scale 1g results (e.g. Mitsch and Clemence 1985). Subsequently, the prediction of the uplift capacity is often not accurate and potentially overestimated, and may not be directly applicable to future larger, higher capacity anchors.

The objective of the paper is to offer insights into potential areas to increase the reliability of semi-analytical approaches for plate and screw anchor design. Results of numerical FE simulations of large diameter plate uplift at different relative embedment ratios and soil conditions are firstly validated with respect to published experimental results. This includes investigation of the resulting failure mechanisms for the different situations. The most commonly used semi-analytical approaches are then compared to the FE results to identify the most suitable method for further development based upon ultimate uplift resistance and how the failure mechanism assumptions compare to those observed in the FEA. Finally, a modified stress distribution along the theoretical failure mechanism is introduced and used to modify the analytical method to take account of the soil compressibility.
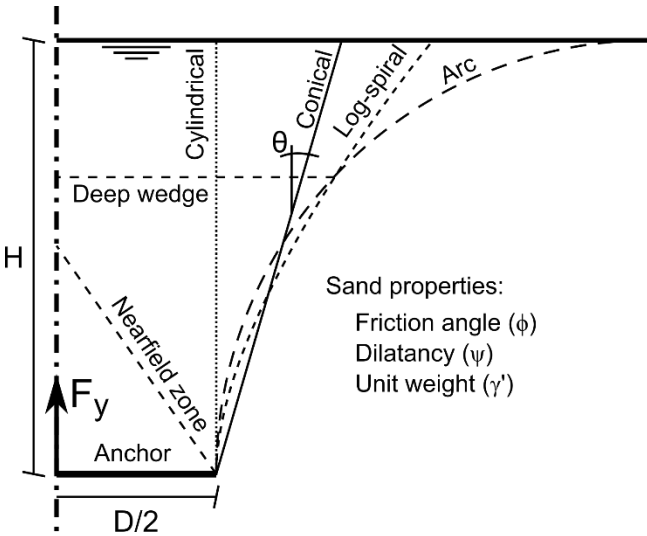
Figure 1 Idealisation of the anchor uplift problem and failure mechanism

2. Numerical simulations

Uplift simulation of plates were carried out using the 2D finite element (FE) software PLAXIS (PLAXIS 2017a) to determine the uplift capacity of deep large diameter plates and validate it against published experimental results. These analyses used a non-linear elasto-plastic constitutive model such that the mobilised stress conditions associated with typical limiting uplift displacements, along with the influence of soil compressibility on these

2

distributions, can be investigated. Wished-in-place circular plates were simulated axisymmetrically under upwards vertical (uplift) loading, to match the conditions assumed in the aforementioned studies.

2.1. Modelling approach

The problem investigated is idealised in Figure 1~~Figure 1~~. The anchor is assumed to be a circular plate of diameter D embedded within sand (peak friction and dilatancy angle: ϕ, ψ, respectively) at a depth H below the ground surface. The anchor consists of a 1.7m diameter horizontal plate. This diameter is representative of upscaled foundations for offshore wind turbines, such as those studied in (Al-Baghdadi et al. 2017a). 5-node plate elements were used to idealise its behaviour. A uniform vertical displacement was imposed all along the plate. Therefore, the plate was assumed to be rigid and the solution does not depend on the plate properties (i.e. bending stiffness). Zero-thickness interface finite elements were included on each side of the plate. They allow the opening of a gap below the anchor when effective normal stresses become equal to zero (i.e. no tension condition).

The soil was modelled by 15-node triangular finite elements. The boundaries were defined far enough from the plate to avoid any boundary effect. The horizontal bottom boundary lay 7D below the anchor and was fully fixed. The vertical boundary was located 17D laterally from the symmetry axis, allowing vertical deformation but fixing horizontal movement. The soil was assumed to be completely saturated with the water level located at the top soil surface, which was free to move. The anchor was modelled at several depths (H), corresponding to relative embedment ratios H/D between 1 and 9. The mesh was chosen to be a good compromise between accuracy of results and cost of simulation. It was different for every geometry, but all meshes were refined in a zone extending horizontally to 3.5 plate diameters from the axis of symmetry encompassing the failure surface. The number of elements ranged from 1767 (respectively 14428 nodes) to 2587 (respectively 21048 nodes) for relative embedment ratios between 1 and 9. An example of the mesh for the deepest embedment (H/D=9) is presented in Figure 4~~Figure 4~~.

The soil behaviour was modelled using the 'hardening soil with small strain stiffness' (HS small) constitutive model (Schanz et al. 1999, Benz 2007) under drained conditions. The soil parameters used were those that have been previously calibrated for Congleton HST95 sand which has two main advantages. Firstly, its parameters were calibrated against laboratory element tests over a wide range of relative densities by Al-Defae et al. (2013). Secondly these parameters have been previously validated against 1g, centrifuge and field tests against various boundary value problems, including static and dynamic loading and for screw piles (Al-Defae et al. 2013, Knappett et al. 2016, Al-Baghdadi et al. 2017).

The HS small model is based on strain hardening of two yield surfaces (Mohr-Coulomb in shear and a cap in compression) with shear and volumetric plastic strain (respectively). Stiffness is confinement dependent and degrades with increasing shear strain. It also encompasses an increase in stiffness during unloading-reloading in comparison to virgin loading. A tension cut-off avoids any pure tension within the soil material. The volumetric behaviour is non-associated and is related to the mobilised dilatancy angle of the soil as reported in (PLAXIS 2017b). A dilatancy cut-off is also included to ensure the current void ratio cannot exceed the maximum possible one defined by e_{max}. The model does not capture post-peak softening at large strains or grain crushing, but has been shown to provide good matches to field test load–displacement data over the working load range in sands for both bored piles (Tolooiyan and Gavin 2013) and continuous helical displacement (CHD) piles (a

3

type of cast in situ concrete screw pile) (Knappett et al. 2016). Strain-softening should decrease the mobilised friction angle in a zone close to the anchor, where shear strain is the largest. Subsequently, if strain softening is significant, the model will overpredict the uplift capacity. However, ~~this~~ the strain-softening zone should remain limited in size, especially at the lower depths. Stiffness should also be modified, but this is not tackled in this study. All parameters are summarised in Table 1~~Table 1~~. Despite the material being cohesionless a very small apparent cohesion of 1kPa was added for numerical stability.

The simulation was composed of several phases. The initial geostatic stress field was firstly generated within the soil and at the interface. The initial coefficient of earth pressure was based on Jaky's formula (Jaky 1944) such that $K_0 = 1 - \sin \phi$. The ~~uniform~~ imposed uniform displacement was then applied to all nodes of the plate.

Soil parameters		Unit	Equation	Dr = 50% I_D=0.5	Dr = 70% I_D=0.7	Dr = 90% I_D=0.9
Min void ratio	e_{min}	[-]		0.469	0.469	0.469
Max void ratio	e_{max}	[-]		0.769	0.769	0.769
Initial void ratio	e_0	[-]		0.618	0.558	0.4972
Friction angle	ϕ	[°]	$20I_D + 29$	39	43	47
Dilatancy angle	ψ	[°]	$25I_d - 4$	8.5	13.5	18.5
Effective cohesion	c	[kPa]	$25I_d + 20.22$	1.0	1.0	1.0
Oedometer stiffness	E_{oed}^{ref}	[MPa]	$25I_d + 20.22$	32.7	37.7	42.7
Secant stiffness	E_{50}^{ref}	[MPa]	$1.25 E_{oed}^{ref}$	40.9	47.1	53.4
Unloading/reloading stiffness	E_{ur}^{ref}	[MPa]	$3 E_{oed}^{ref}$	90.66	105.5	128.2
Material parameter	M	[-]	$0.6 - 0.1\,I_D$	0.55	0.53	0.51
Unloading/reloading Poisson's ratio	ν_{ur}	[-]		0.2	0.2	0.2
Reference shear strain	$\gamma_{0.7}$	[-]	$(1.7I_d + 0.67) \cdot 10^{-4}$	$1.52 \cdot 10^{-4}$	$1.86 \cdot 10^{-4}$	$2.2 \cdot 10^{-4}$
Low strain shear modulus	G_0^{ref}	[MPa]	$50I_D + 88.8$	113.8	123.8	133.8
Total unit weight	γ_{tot}	[kN/m³]	$30I_d + 14.5$	19.7	20.06	20.42

Table 1 Calibration of the HSsmall parameters for the HST95 Congleton sand, after (Lauder 2010, Al-Defae et al. 2013, Al-Baghdadi et al. 2017a), reference stiffnesses are for a reference pressure equal to p^{ref} = 100kPa

2.2. Validation

The tensile (uplift) load at failure F_y is often expressed as a non-dimensional bearing factor N_γ,

$$[1] \qquad N_\gamma = \frac{F_y}{\gamma' A H}$$

where γ' is the buoyant unit weight of the sand and A=π D²/4 is the surface area of the plate.

Results collected from the literature for 1g, centrifuge or field tests show an increasing bearing factor with the relative embedment ratio H/D. The results demonstrate a range of potential N_γ values for a given H/D based upon previous studies with this range becoming larger as H/D increases (i.e. for deeper or higher capacity anchors). For instance, N_γ related to peak friction angles ranging from 40° to 50° and H/D=6, may vary between 19 and 80. In general, larger diameter and centrifuge tests provide a lower bound for the results (Schiavon et al. 2016, Giampa et al. 2017, Perez et al. 2017) while the very small-scale tests tend to provide larger bearing factors (Baker and Konder 1966, Mitsch and Clemence 1985, Murray and Geddes 1987, Ghaly et al. 1991). The larger capacity of small-scale tests may be explained by dilatancy which is more pronounced due to low confining stress as suggested by Bradshaw et al. (2016).

Most analytical criteria distinguish between shallow and deep failure mechanisms. In the shallow case, the failure surface defines a wedge of soil extending from the edge of the plate up to the soil surface (Mitsch and Clemence 1985, Ilamparuthi and Muthukrishnaiah 1999, Liu et al. 2012). In the second case the failure mechanism is a plastic flow and cannot be detected from the surface. For the range of friction angles 40°-50°, there is no clear transition between deep and shallow mechanisms, marked by a plateau of N_γ. For this range of friction angles, the critical H/D could be anywhere from 5 to 10.

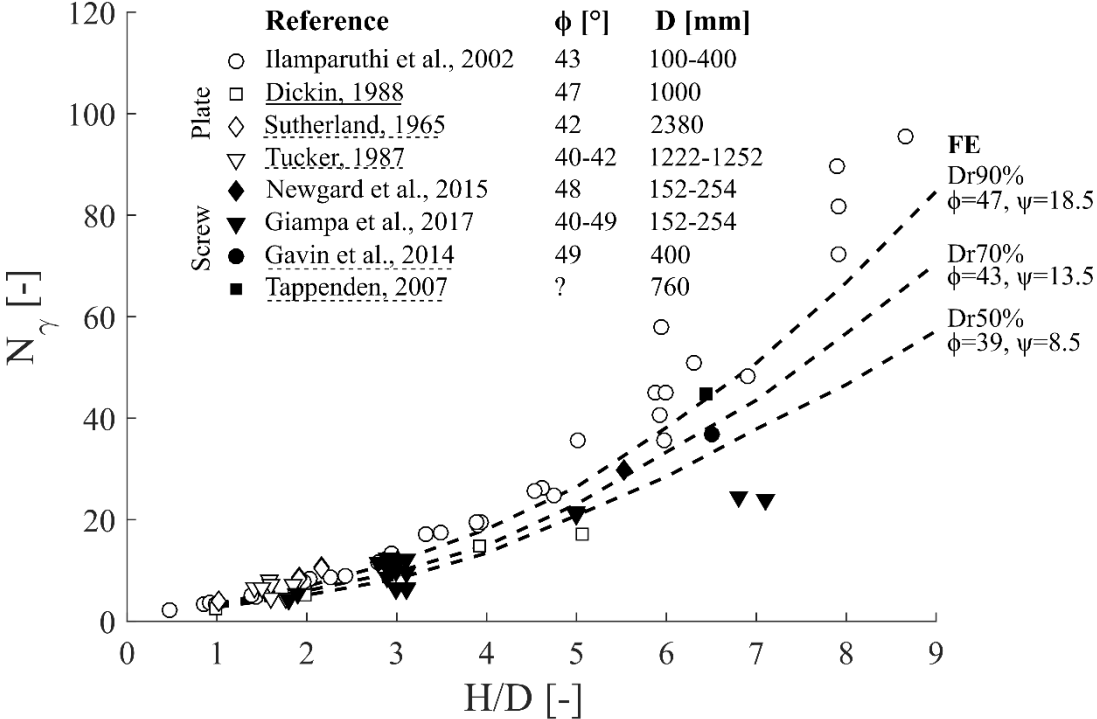|	Reference	ϕ [°]	D [mm]
○	Ilamparuthi et al., 2002	43	100-400
□	Dickin, 1988	47	1000
◇	Sutherland, 1965	42	2380
▽	Tucker, 1987	40-42	1222-1252
◆	Newgard et al., 2015	48	152-254
▼	Giampa et al., 2017	40-49	152-254
●	Gavin et al., 2014	49	400
■	Tappenden, 2007	?	760

Figure 2 Validation of FE simulations with respect to relatively large scale 1g, centrifuge and field experimental results, for plate anchors (open markers) and screw anchors (closed markers)

FE simulations were carried out for three sand relative densities (50%, 70%, 90%) whose peak friction angles range from 39° to 47°. They are validated against relatively large scale, centrifuge and field tests results, as depicted in Figure 2Figure 2, in order to avoid discrepancies due to low confining stress levels in 1g small-scale test data. Results from screw anchors (Schiavon et al. 2016) and (Perez et al. 2017) were not reported since the authors report a different failure mechanism than expected for plates due to the particular type of installation disturbance induced. The results of Dickin (1988) were obtained for square plates, whose uplift capacity is proven to be lower than the circular plates (Giampa et al. 2018). For numerical simulations, failure is defined when the load-displacement relationship reaches a plateau and a failure mechanism is fully formed (shear band extending to the surface, no flow around was observed).

The FE simulation results fit relatively well with the general trend of experimental data and reflect the non-linear increase of N_γ with H/D. Results from Ilamparuthi et al. (2002) are slightly greater than the numerical results for identical strength parameters, especially at larger embedment. This could be due to the relatively small size of the model anchors compared to others within this dataset. Results of Tucker (1987) are also greater but they are obtained from belled piles during field tests. Results from Giampa et al. (2017) are below the

numerical results, especially at low friction angles or large embedment. The sand material used for these experiments possessed particularly high strength parameters given the low relative densities between 14% to 45%, depending on the test and depth investigated (Schneider et al. 2016, Giampa et al. 2017). It is believed that this relatively loose state (and corresponding lower stiffness) modifies the final capacity due to a compression effect within the soil, as will be discussed in detail later. The underprediction of the Giampa approach at larger embedments has been recently shown by Rasulo et al. (2017), through small-scale 1g tests.

The centrifuge tests of Dickin (1988) are slightly lower than the numerical results, which is probably due to their square shape, while field tests (Sutherland 1965, Tappenden 2007, Gavin et al. 2014) are generally in agreement.

Shear strain is shown in Figure 3~~Figure 3~~ for several simulations at various relative embedment ratios H/D and the three investigated relative densities. The maximum shear strain was limited to 30% for clarity, though it could be larger locally. Results plotted correspond to the time step where the peak uplift load occurs in the load-displacement relationship. The theoretical failure surface proposed by Giampa et al. (2017), which is inclined at approximately the angle of dilation with respect to the vertical, is superimposed (red dashed line) on these results. At shallow embedment, the numerically observed failure surface is almost identical to the theoretical one, confirming the hypothesis made by Giampa et al. (2017). However, it diverges from the theoretical one as embedment increases. This is consistent with fault reverse rupture propagation centrifuge experiments and numerical simulations reported by Anastasopoulos et al. (2007). The divergence is a function of the relative density or peak friction angle and embedment. The relative embedment (H/D) at which the surface deviates from a straight line is approximately equal to 3.5, 4.5 and 5.5 for soil densities respectively equal to 50%, 70% and 90%. However, this should not be considered as a shallow/deep transition (c.f. Figure 3), as the failure mechanism reaches the ground surface for each case considered, though vertical displacement at the soil surface is low.

Although the failure mechanism reaches the ground surface for each case considered, there is a clear change in the shear-strain pattern as embedment increases. A new diffuse shear band appears starting from the edge of the plate but inclined towards the axis of symmetry. It forms an approximately conical soil block (referred to hereafter as a 'nearfield zone'), similar to the one forming beneath a shallow footing (Prandtl 1921, Knappett and Craig 2012). The theoretical boundary of this zone ($45^{o}+\phi/2$) is drawn in Figure 3~~Figure 3~~ for comparison but does not exactly correspond to numerical results. Shear deformation above this conical zone increases significantly with embedment and decreases with increasing density. This is related to increasing displacement required to reach the peak load (almost 1m for the D_r =50%, H/D=9 case).
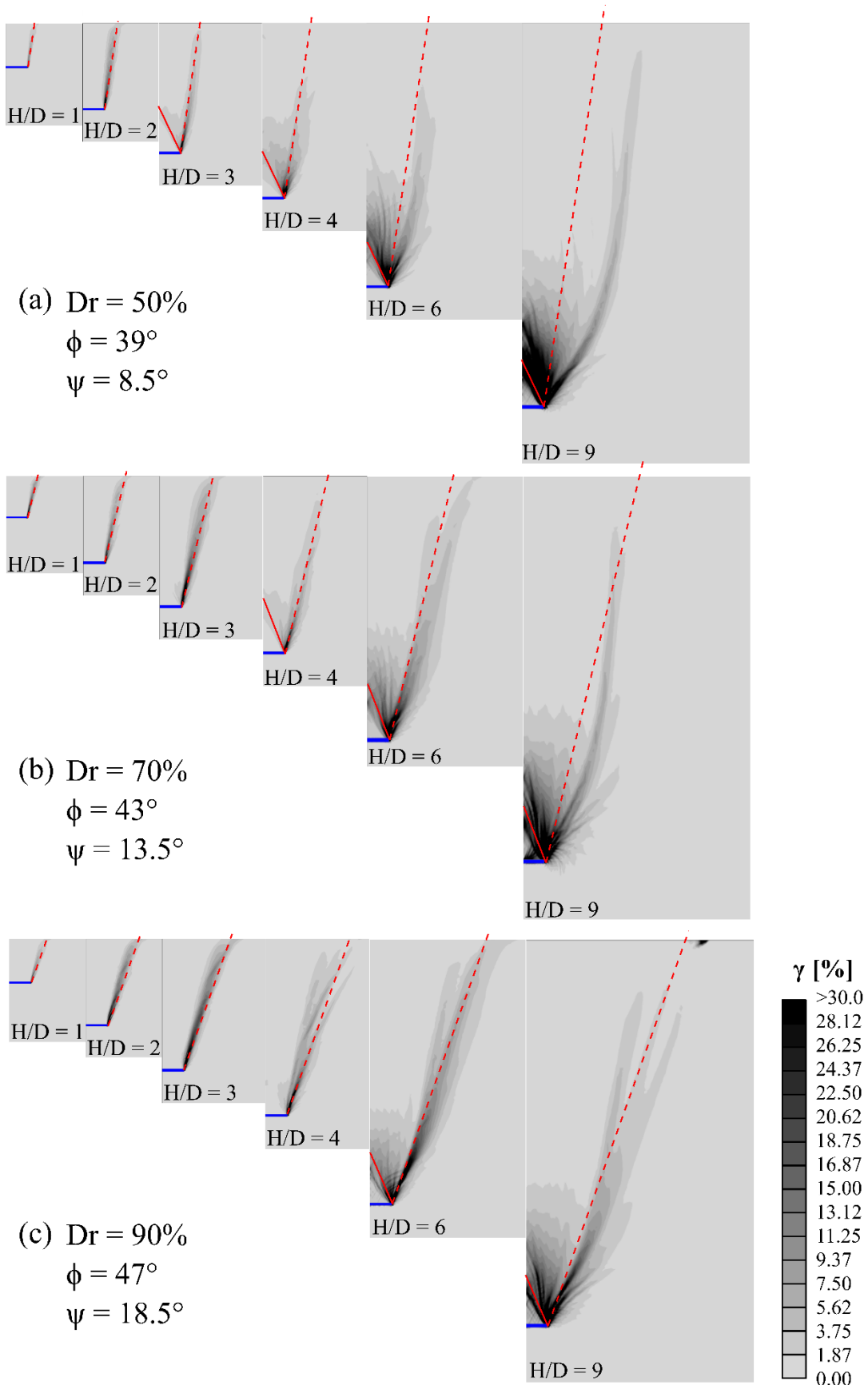
Figure 3 Comparison of shear strain (γ) contours obtained numerically for plate anchor (D = 1.7m) at three densities and several relative embedment ratios (variable H), the horizontal solid blue line is the anchor, red dashed lines indicate an assumed failure plane inclined at the dilatancy angle to the vertical

8

direction, red solid lines delineate the mechanism inclined at 45+ϕ/2 to the horizontal, figures (a-c) represent simulation results at three different densities described in **Table 1**~~Table 1~~

3. Comparison to analytical capacity models

In the following section several existing analytical anchor capacity models are systematically reviewed. Their methodologies, equations and key hypotheses are summarised. They are then compared to the previously validated numerical results.

3.1. Models, equations and hypotheses

Several models have been developed over the last 50 years to assess the uplift capacity of anchors in drained cohesionless materials. Most analytical criteria considered are based on the variables (geometry and soil properties) defined in [Figure 1](#)~~Figure 1~~ as well as an assumption on the failure mechanism shape. The different shapes considered (cylindrical, conical or log-spiral) are shown indicatively in [Figure 1](#)~~Figure 1~~. The variable θ is the inclination of the slip surface to the vertical in the specific case of a conical (linear) failure surface. For deep mechanism cases, H_0 is the height (above the anchor) over which the failure mechanism develops. Some additional variables are included within the different methods as outlined below.

Vesic et al. (1965) studied the problem of an explosive point charge expanding a cavity in a homogeneous and isotropic solid. Results of this cavity expansion modelling was used to compute the breaking pressure of a spherical expansion in a semi-infinite medium representative of the ocean bottom (Vesic 1969, 1971). In this work, the bearing factors for cohesionless soils are provided as a function of the relative embedment and friction angles for shallow anchors (for H/D≤5). This data was extrapolated for greater embedment depths. The soil shear resistance and the soil weight are included within this formulation.

Meyerhof and Adams (1968) assumed the failure surface is a truncated cone starting from the edge of the anchor, along which a general shear failure exists. The problem was simplified by considering the total passive earth pressure inclined at an angle from the horizontal equal on average to 2/3ϕ and acting along a cylindrical surface starting from the anchor's outer edge. Earth pressure coefficients were obtained from the Caquot and Kerisel tables (Caquot and Kerisel 1948). Finally, a shape factor and the coefficient of passive earth pressure acting on the vertical plane were gathered within a single empirical factor sK_u provided in a chart, based on comparison with experimental results. Another approach proposed by Das and Shukla (2013) consisted of approximating $K_u = 0.95$ and calculating the shape factors as a function of the friction angle and relative embedment ratio. The total uplift capacity was then composed of the soil weight (computed as a truncated cone), shear mobilised along an inclined failure surface (if shallow $H_0=H$) and an overburden term activated only when the anchor has a deep failure mode ($H_0<H$). The transition between shallow and deep failure modes was provided in the original paper as a function of the peak friction angle. The authors recommended an average failure surface inclination equal to $\phi/3$. The general equation of the uplift strength is written as follows (Meyerhof and Adams 1968)

[2]
$$F_y = \frac{\pi}{3}\gamma'H\left[\left(\frac{D}{2}+H_0\tan\theta\right)^2 + \frac{D}{2}(D+H_0\tan\theta)\right]$$
$$+ \frac{\pi}{2}\gamma'DH_0(2H-H_0)\,sK_u\tan\phi + \pi\gamma'\left(\frac{D}{2}+H_0\tan\theta\right)^2(H-H_0)$$

9

Mitsch and Clemence (1985) proposed a criterion dedicated to screw anchors. It was assumed that the top plate/helix lifted a truncated cone of soil (inclined at $\phi/2$ to the vertical) in the case of a shallow failure mode. The total uplift strength is composed of the weight of the soil and friction mobilised along the inclined failure surface,

[3]
$$F_y = \frac{\pi}{3} \gamma' H \left[\left(\frac{D}{2} + H_0 \tan \theta \right)^2 + \frac{D}{2} (D + H_0 \tan \theta) \right] \\ + \pi \gamma' K_u \tan \phi \cos^2 \phi \left(\frac{D^2 H^2}{2} + \frac{H^3 \tan \phi}{3} \right)$$

The K_u coefficient is similar to the one used by Meyerhof and Adams (1968) but reduced values are considered to take into account a disturbance effect due to installation. The deep mechanism anchor capacity is the sum of a bearing factor N_{qu} (provided in a chart) and the shear friction mobilised along the shaft, as follows,

[4]
$$F_y = \frac{\pi \gamma' D^2}{4} H N_{qu} + \frac{\pi \gamma' D H^2}{2} K_u \tan \phi$$

Murray and Geddes (1987) introduced a general formulation of the uplift capacity of plate anchors, based on a log-spiral failure surface. The solution depends on the inclination of the failure surface at the edge of the anchor θ, the inclination α of an equivalent plane surface, the inclination of the resultant weight and friction loads to the vertical β and a coefficient of lateral earth pressure K_t such that

[5]
$$F_y = \frac{\pi \gamma' H D^2}{4} + \frac{\pi}{2} \gamma' H^2 \frac{\tan \theta - \tan \beta}{\tan \beta - \tan(\phi - \alpha)} \left[D + \frac{2}{3} H (\tan \theta + K_t \tan(\phi - \alpha)) \right]$$

The authors assumed that $\theta = \alpha = \phi/2$, which implicitly defines the failure surface as a plane. They also made the hypothesis that $\beta = 3/4\phi$ on average and that $K_t = K_0$, where K_0 is the initial coefficient of earth pressure.

Saeedy (1987) introduced a semi-analytical solution for plate anchors, based on a log-spiral failure surface. The equilibrium equation was solved numerically and results were provided in a chart as a function of the relative embedment ratio and friction angle. A 'compaction factor' was introduced to take into account progressive shear mobilisation of the material and gradual packing of the soil. Indeed, the true soil behaviour is not rigid-plastic as conveniently assumed for analytical solutions but requires a certain amount of shear deformation to mobilise its peak friction angle. The strain and stress field are then modified within the soil where the failure mechanism develops. This in turns increases effective normal stress on the failure surface resulting in mobilisation of larger shear stresses.

Ghaly et al. (1991) developed an analytical criterion based on an extensive dataset of small-scale experiments for screw anchors. Similarly to previous authors, they assumed a straight inclined failure surface reaching the top soil surface (shallow mode) or limited to a given height H_0 above the anchor (deep mode). The uplift capacity is composed of the weight of the uplifted soil, shear component along failure surface (shallow) and overburden component (deep mode) such that,

10

$$F_y = \frac{\pi}{3}\gamma'H\left[\left(\frac{D}{2} + H_0\tan\theta\right)^2 + \frac{D}{2}(D + H_0\tan\theta)\right]$$

[6]
$$+ \frac{\pi}{2}\gamma'K_p'H_0(2H - H_0)\frac{D + H_0\tan\phi}{\cos\theta}\tan\phi_{mob}$$

$$+ \pi\gamma'\left(\frac{D}{2} + H_0\tan\theta\right)^2(H - H_0)$$

The solution depends mainly on a single parameter ϕ_{mob} which was described as an average mobilised friction angle along the failure surface. The earth pressure coefficient K_p' was computed according to this value and was provided in a chart as a function of the friction angle and relative embedment ratio. The inclination of the conical surface θ has a maximum value of $2/3\phi$ which was adopted in Das and Shukla (2013). The maximum radius of the conical surface at the ground surface is bounded by a maximum value dependent on the friction angle (Das and Shukla 2013).

Giampa et al. (2017) recently proposed a new criterion that extended previous work of White et al. (2008) for uplift resistance of pipelines. It is based on the hypothesis that a straight failure surface is inclined to the vertical at an angle θ equal to the dilatancy angle ψ of the soil material. The effective normal stress distribution along the failure surface is based on the hypothesis that the normal shear stress distribution is a function of the dilatancy and peak friction angles. A key advantage of this method is that there is no back-fitted empirical coefficient involved in the formulation,

[7]
$$F_y = \frac{\pi}{3}\gamma'H\left[\left(\frac{D}{2} + H_0\tan\theta\right)^2 + \frac{D}{2}(D + H_0\tan\theta)\right]$$

$$+ \frac{\pi}{2}\gamma'H^2\cos(\phi - \psi)(\tan\phi - \tan\psi)\left(D + \frac{2}{3}H\tan\psi\right)$$

The main features of the different criteria considered are summarised in Table 2Table 2. This shows that despite some similarities, there is no real agreement on the exact type and inclination of the failure surface for shallow failure modes. Neither is there agreement on the shallow to deep failure mode transition. None of these criteria, except the one proposed by Giampa et al. (2017), takes into account the dilatancy angle in the definition of the failure mechanism geometry. Most assume a rigid-perfectly plastic behaviour of the soil, neglecting any potential reduction of the failure surface length due to the vertical displacement of the anchor and any soil volumetric compression. Most importantly, many of them incorporate a back-fitted empirical factor based on comparison with experimental results, mainly small-scale 1g tests.

Study	Anchor type	Theory	Surface Type	Surface Angle θ	Empirical Factor	Dilatancy
(Vesic 1969)	Plate	C.E.	Torus			No
(Meyerhof and Adams 1968)	Plate	L.E.	Cylindrical/ Conical	$\phi/3$	sK_u	No
(Mitsch and Clemence 1985)	Screw	L.E.	Conical	$\phi/2$	sK_u	No
(Murray and Geddes 1987)	Plate	L.E.	Log-spiral/ Conical	$\phi/2$	β, K_t	No
(Saeedy 1987)	Plate	L.E.	Log-spiral		μ	No
(Ghaly et al. 1991)	Screw	L.E.	Conical	$2/3\phi$	ϕ_{mob}	No
(Giampa et al. 2017)	Screw	L.E.	Conical	ψ		Yes

Table 2 Comparison of methodologies and hypotheses of different analytical criteria available in the literature, C.E.= Cavity Expansion, L.E. = Limit Equilibrium

3.2. Results

Comparisons of numerical and analytical criteria are reported in Figure 5Figure 5 and Figure 6Figure 6 for two sets of parameters corresponding to the two extreme relative densities considered here (D_r=50/90%), having (ϕ,ψ)=(39°, 8.5°) and (47°,18.5°), respectively. The estimated bearing factors obtained from the different analytical models are not in close agreement, which may be linked to the differences between the experimental results used for their calibration of the original analytical approaches (Figure 2).
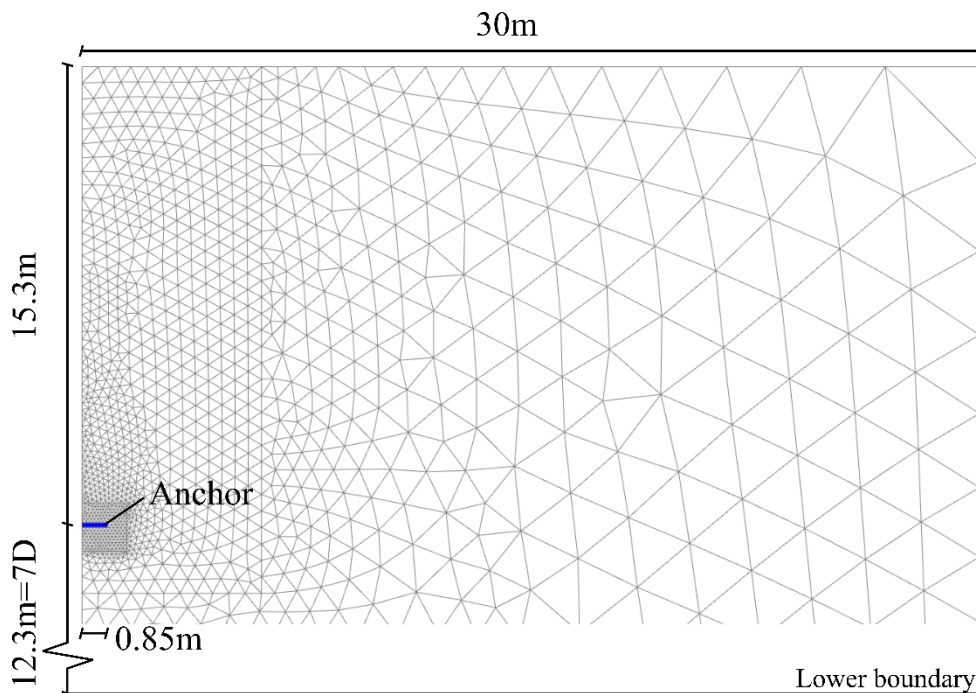

Figure 4 Example of the mesh for a relative embedment ratio H/D=9. The figure only represents a part of the mesh to emphasise the mesh refinement around the anchor.

The criteria described by Ghaly et al. (1991) and Das and Shukla (2013) as well as Mitsch and Clemence (1985) lie mostly above the other results and the numerical simulation undertaken here. This is surprising since these two criteria were developed for screw anchors where there may be some effect of installation disturbance within the empirical factors used. Such disturbance was observed by Perez et al. (2017). Another study (Jeffrey et al. 2016) reported

increase or decrease of soil density around CHD piles, caused by the combination of cavity expansion and installation disturbance, depending on the initial soil density. Mitsch and Clemence (1985) explicitly mentioned that the lateral earth pressure coefficient is decreased with respect to the solution of Meyerhof and Adams (1968) to take into account a disturbance effect due to anchor installation. The high bearing factors predicted by these criteria is thought to be due to the small-scale experimental results against which they were validated and the dilation associated with the high friction angles adopted for comparison. Subsequently, the empirical factors calibrated against these small-scale experiments, lead to the overestimation of the uplift capacity at a larger scale.

The model proposed by Meyerhof and Adams (1968) overestimates the numerical results at larger friction angles but is closer at lower friction angles. The shallow/deep transition is noted in the (39°, 8.5°) case at H/D=6 (Figure 5Figure 5a), while such a transition in N_γ was not observed from the numerical results. Recent results presented by Rasulo et al. (2017) show that the deep mechanism for a similar sand should be attained at a deeper relative embedment (H/D=6-8). The model proposed by Murray and Geddes (1987) overpredicts the bearing capacity at shallow embedment but the difference is reduced with depth. Finally, the criteria of Vesic (1969), Saeedy (1987) and Giampa et al. (2017) tend to underpredict the numerical results at high H/D. However, at shallow embedment (H/D<4), the last two approaches provide a very good estimate of the values obtained numerically, for both sets of soil properties.

In summary, none of the existing models are entirely reliable across the full range of soil properties and relative embedment ratios considered here. At shallow depths, the criteria of Giampa et al. (2017) and Saeedy (1987) predict bearing factors consistent with numerical and experimental results at larger scale or in centrifuge tests. The criterion of Murray and Geddes (1987) also appears to be able to capture the behaviour at larger embedment ratios.

13
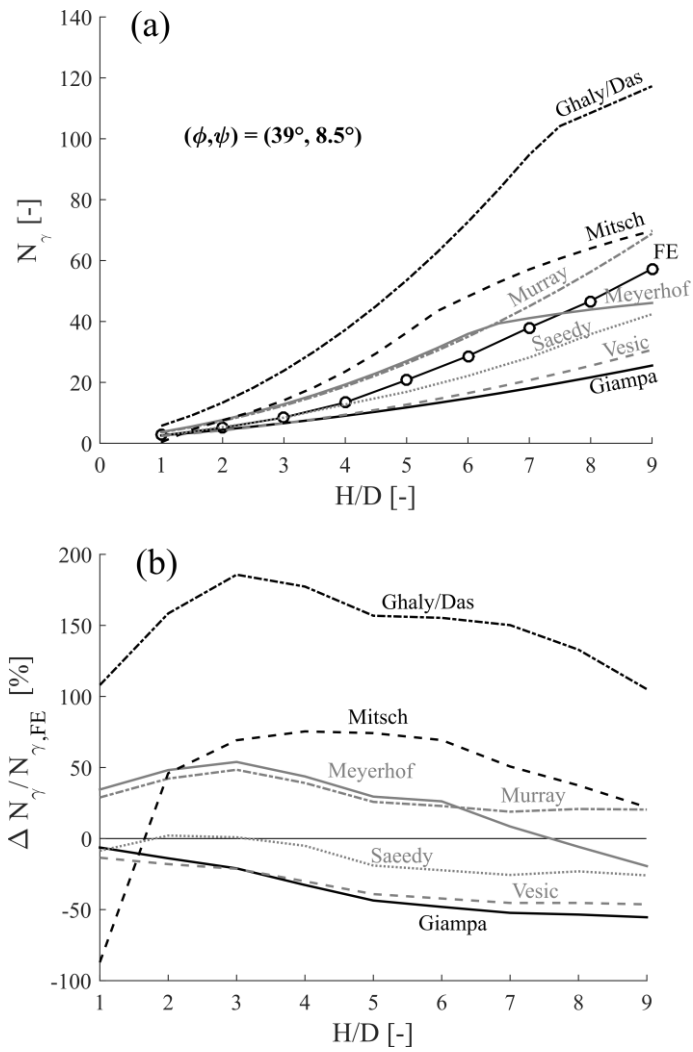
Figure 5 Comparison of analytical criteria with numerical FE simulations, HST95, Dr =50%
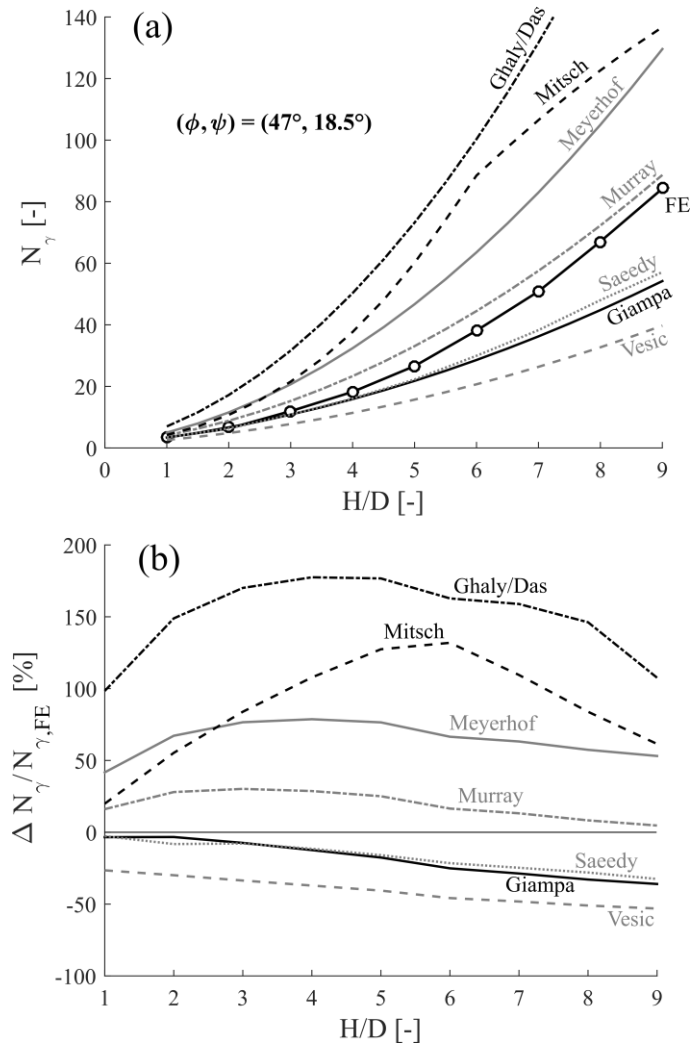
Figure 6 Comparison of analytical criteria with numerical FE simulations, HST95, Dr =90%

4. Effect of soil compressibility

The recent Giampa criterion (Giampa et al. 2017) has been shown to be consistent with numerical simulations at shallow depths as well as experimental results. The postulated shallow failure mechanism was observed numerically and consists of a shallow conical surface, initiating from the plate edge up to the surface, whose inclination to the vertical is equal to the dilation angle. Its different hypotheses are reviewed to explain why it underpredicts the finite element simulations at larger depths.

4.1. Stress distribution along the assumed failure surface

The comparison of bearing factors N_γ obtained numerically (FE) or analytically (Giampa et al. 2017), reveals that the difference with respect to numerical results increases almost linearly from -3% (H/D=1) to -25% (H/D=6), as reported in Figure 6Figure 6b. However, over this range of embedment, the failure surface observed numerically in Figure 3Figure 3 is almost straight and inclined at $\theta = \psi$, which corresponds to the hypothesis of Giampa et al. (2017). Therefore, the difference of N_γ does not appear to be associated with the shape of the failure surface or a shallow/deep transition.

15

All analytical approaches are based on an assumption ~~on~~ about the stress distribution along the failure mechanism. In the following, it has been considered that the failure mechanism postulated by Giampa et al. (2017) was correct, even if the true failure surface diverges at larger embedment. The numerical effective normal stress, σ'_N and shear stress, τ distributions along this assumed failure surface (red dashed line in Figure 3~~Figure 3~~) were traced from numerical results and for a given time step, corresponding to the peak or plateau of the load-displacement relationship. These distributions are different from the linearly increasing relationship assumed in most analytical approaches.

Figure 7~~Figure 7~~ represents the ratio of the numerical (τ) to the analytical (τ_G) shear stress distribution along the failure surface for a relative embedment ratio H/D=5, at the three densities. The horizontal axis represents a curvilinear coordinate s along the failure plane starting from the edge of the plate up to the surface and normalised with respect to plate diameter. The Giampa criterion assumes the shear stress distribution at failure along the cross-section increases linearly with depth and is described by the following equation,

[8] $$\tau_G = \tan\phi \cos(\phi - \psi)\,\gamma' z = \tan\phi \cos(\phi - \psi)\,\gamma'(H - s\cos\psi)$$

where z is the depth and s is the coordinate along the failure mechanism. Figure 7~~Figure 7~~ shows that shear stress reaches a peak close to the plate edge $\left(\frac{s}{D} \approx 0.5\right)$ where it is over~~almost~~ 3 times greater than the assumed value. It decreases afterwards and tends towards the assumed distribution close to the soil surface $\left(by\ \frac{s}{D} \approx 3\right)$. This increase in shear stress is similar in shape to the increase in the normal effective stress σ'_N distribution along the failure surface. Neglecting this effect in Equation (8) leads to underestimation of the uplift strength and bearing capacity in the Giampa criterion.
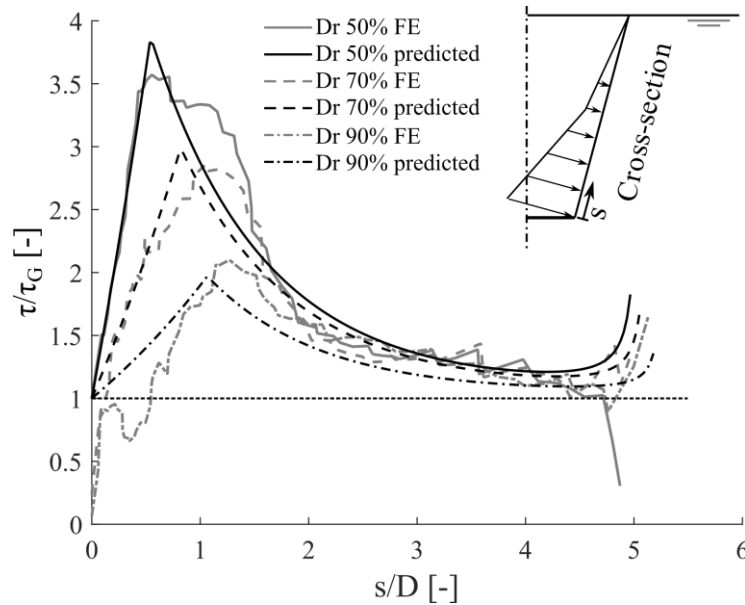

Figure 7 Cross-section of the ratio of shear stress τ from FE simulations (grey) or predicted distribution (black) to the assumed Giampa value τ_G, along a plane emanating from the edge of the plate and inclined at ψ degrees to the vertical, H/D=5

Most of the analytical approaches consider that failure occurs between two rigid solid blocks, which is not the case for the finite element simulations. Therefore, the difference in stress distribution along the failure mechanism can be idealised as shown in Figure 8~~Figure 8~~.

Although real sand materials exhibit post-peak softening during shear stress, none of the analytical approaches considers it, therefore the shear stress-strain relationship is idealised as perfectly plastic after peak. The maximum shear stress that can be mobilised increases with depth as well as the <u>effective</u> normal stress. The rigid body movement induces that the relative displacement or shear strain (γ_f) is constant all along the failure mechanism. Therefore, shear stress is mobilised simultaneously all over it (limit analysis) or progressively from the top if a strain-hardening behaviour is considered within the interface.

On the contrary, a deformable wedge involves a gradient of vertical strain, maximum just above the anchor and minimum at the soil surface. The vertical strain mechanically induces lateral strain, both generating an increase in confinement and <u>effective</u> normal stress ($\Delta\sigma'_N$) close to the anchor. This in turn increases the maximum shear stress that could be mobilised. Finally, the shear strain all along the failure mechanism is not constant but increases with depth.

This enhancement in mobilised normal/shear stress on the shear plane related to the soil compressibility was previously recognised by Vesic (1969) who introduced a compressibility factor I_r in his bearing factor formulation.

<u>Figure 9</u>~~Figure 9~~ depicts the volumetric strain ϵ_v, the vertical σ'_v and horizontal σ'_h stress distributions for H/D=4 and D_r=90%. Volumetric strain results in soil dilatancy along the failure mechanism (ϵ_v>0) and also soil compression above the anchor. Both vertical and horizontal stress distributions are modified due to the soil-plate contact. They both increase significantly with respect to the initial stress state ($\sigma'_{v0} \approx 70$kPa at the depth of the plate). The increase of the vertical stress is mainly located above the plate and only slightly influences the failure surface, while the horizontal stress is modified within a zone that intersect the failure mechanism, providing the enhancement in <u>effective</u> normal stress σ'_N observed along the cross-section.
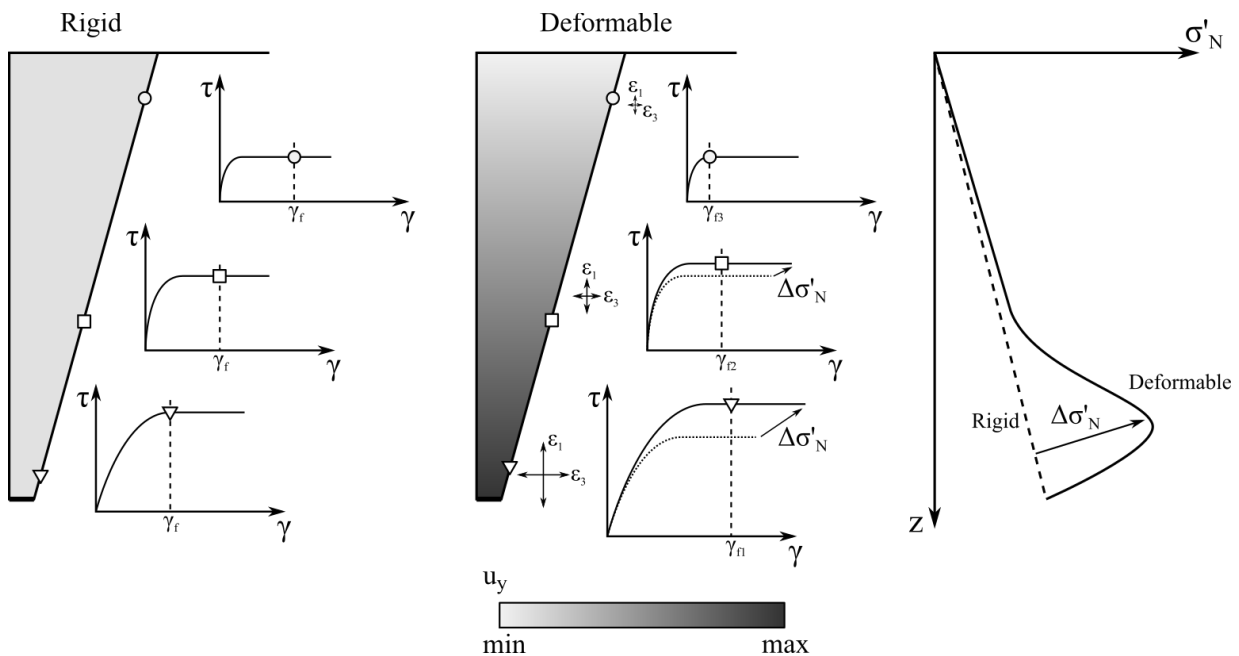

Figure 8 Comparison of idealised shear stress mobilisation between rigid and deformable wedge uplifted by a plate anchor
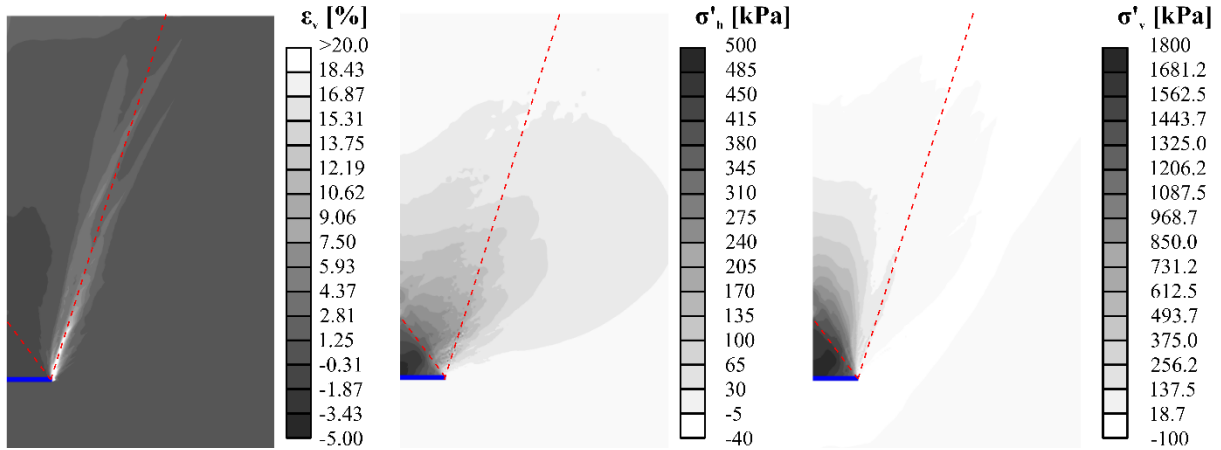
17

Figure 9 Contours (absolute value) of volumetric strain ϵ_v, horizontal σ'_h and vertical σ'_v cartesian effective stresses (compression positive), relative embedment H/D=4 and relative density Dr =90%, the red dashed lines indicate the inclination of the plane inclined at $\psi = 18.5°$ to the vertical

4.2. Analytical approximation of the shear stress distribution

The shear and effective normal stress data along the failure surface in each numerical simulation were imported in Matlab to be post-processed and compared. The analysis of the shear stress distribution at all relative embedments and densities leads to the following conclusions:

- The shear stress distribution can be idealised as the sum of the original Giampa linear distribution (Equation 88) and an additional component as shown schematically in Figure 10Figure 10.
- The additional component may be idealised as a linear increase of τ up to τ_{peak} at a distance s_{peak} from the anchor edge and an exponential decrease with increased s post-peak. The use of an exponential function to describe the degradation of shear stress has been adopted following the approach for pile shafts proposed by Randolph 2003.
- The additional component becomes negligible at a relative distance s/D>3 after the peak stress, where the original Giampa stress distribution is adopted.
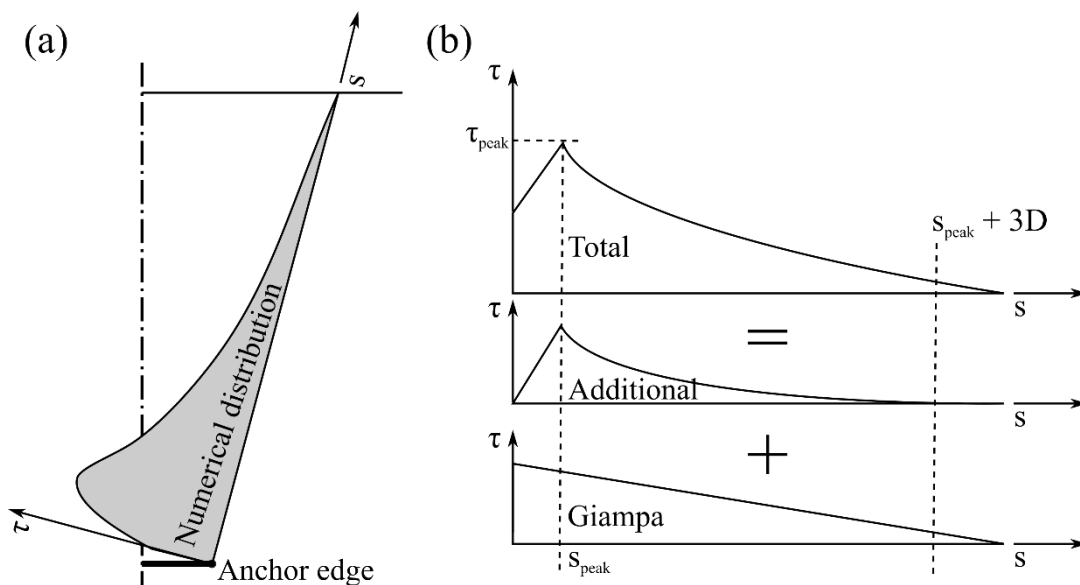

Figure 10 Idealisation of the shear stress distribution along the failure mechanism as the sum of the original Giampa shear stress distribution plus a peak distribution; (a) shear stress -τ- along the inclined

18

cross-section of curvilinear coordinate -s-; (b) decomposition of the shear stress distribution in two components and identification of peak stress

The peak total shear stress was identified for each numerical simulation. Results were normalised with respect to the initial vertical effective stress σ'_{v0} and friction angle and are displayed in Figure 11~~Figure 11~~. For each density, the normalised peak shear stress is almost equal to one at shallow relative embedment. It then begins increasing almost linearly with H/D from a threshold, equal to H/D=3.1, 3.7 and 4.5 for relative densities equal to 50%, 70% and 90% respectively. This threshold corresponds to the appearance of the additional nearfield zone immediately above the anchor shown in Figure 6. The increase in peak shear stress appears to be more significant at the lowest density where the soil is more compressible (lower stiffness from Table 1).

Figure 12~~Figure 12~~ shows the normalised distance from the plate edge ($\xi_{peak}=s_{peak}/D$) at which the peak shear stress τ_{peak} occurs. Numerical results are more variable in this case. However, it appears that this distance increases almost linearly from 0 (the peak is located directly at the plate edge) to a limiting value at larger H/D (equal to 4.0, 4.6 and 6.4 for relative densities equal to 50%, 70% and 90% respectively). Though these transition limits compare well with the critical embedment ratios reported in the literature, they do not correspond to a shallow to deep failure mechanism transition. Indeed, as reported in Figure 3~~Figure 3~~, the failure mechanism observed always reaches the soil surface. The total shear stress distribution can be analytically defined for each density and relative embedment ratio as

$$[9] \qquad \tau(\xi) = \begin{cases} \tau_{G0} + \dfrac{\tau_{peak} - \tau_{G0}}{\xi_{peak}}\xi, & \xi \le \xi_{peak} \\ \tau_G(\xi) + \left(\tau_{peak} - \tau_{G,peak}\right)\exp\left[-\kappa\left(\xi - \xi_{peak}\right)\right], & \xi \ge \xi_{peak} \end{cases}$$

where $\tau_G(\xi)$ is the assumed Giampa distribution, τ_{G0} and $\tau_{G,peak}$ are the values of this function for $\xi = 0$ and $\xi = \xi_{peak}$ respectively, τ_{peak} is the maximum shear stress obtained from the linear best-fit in Figure 11~~Figure 11~~ for given H/D and density, and ξ_{peak} is the normalised distance at which the maximum shear stress is measured obtained from the linear best-fit in Figure 12~~Figure 12~~. The κ value controls the degradation rate of the exponential function. As previously mentioned, the peak stress distribution vanishes at a distance approximately equal to 3 plate diameters after peak:

$$[10] \qquad \exp\left[-\kappa\left(\xi - \xi_{peak}\right)\right] = \exp[-3\kappa] \le C$$

where C is a constant. Considering a value of C equal to 0.03 provides a good overall approximation of the shear stress distribution. Therefore, κ is equal to 1.17. For H/D lower than 3, $\xi = H/D$ should be used in Equation [10~~[10~~], while ξ_{peak} is obtained from Figure 12~~Figure 12~~.

The proposed semi-analytical shear stress distribution is compared to the finite element results in Figure 7~~Figure 7~~. Results are normalised with respect to the Giampa et al. (2017) distribution. It shows that the overall shape of the stress distribution (peak stress and decreasing rate) is consistent with the finite elements results. The end of the distribution seems to diverge, but this is an artefact of the normalisation, as the Giampa distribution tends to very small values close to the surface.

19

Similar conclusion could be drawn on the distribution of the normal effective stress along the failure mechanism. Both of these distributions can be used to improve the prediction of existing failure criteria, through the addition of a correction factor.
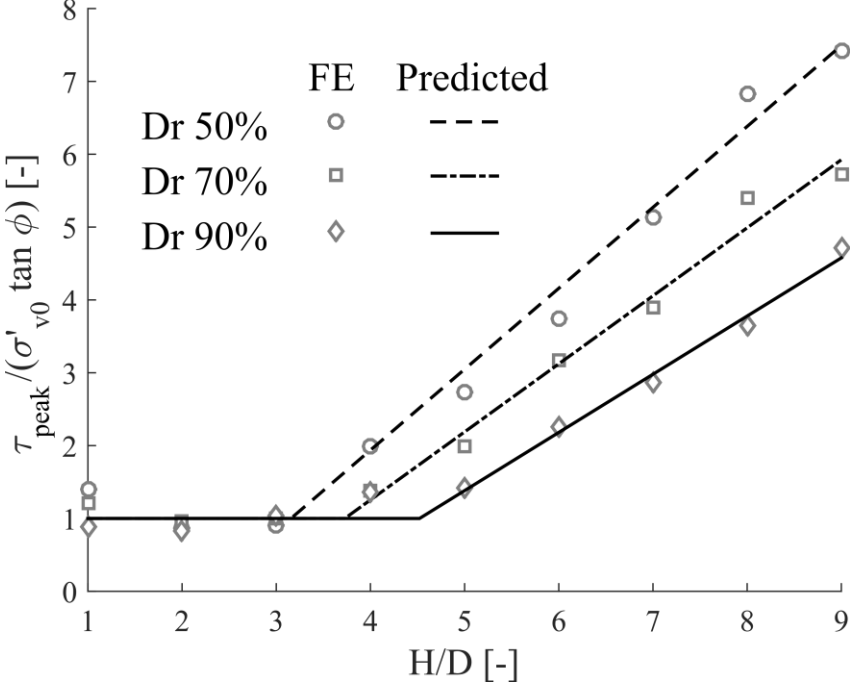

Figure 11 Normalised peak shear stress along the failure mechanism as a function of density and relative embedment ratio, numerical results (markers), best-fit (curves)
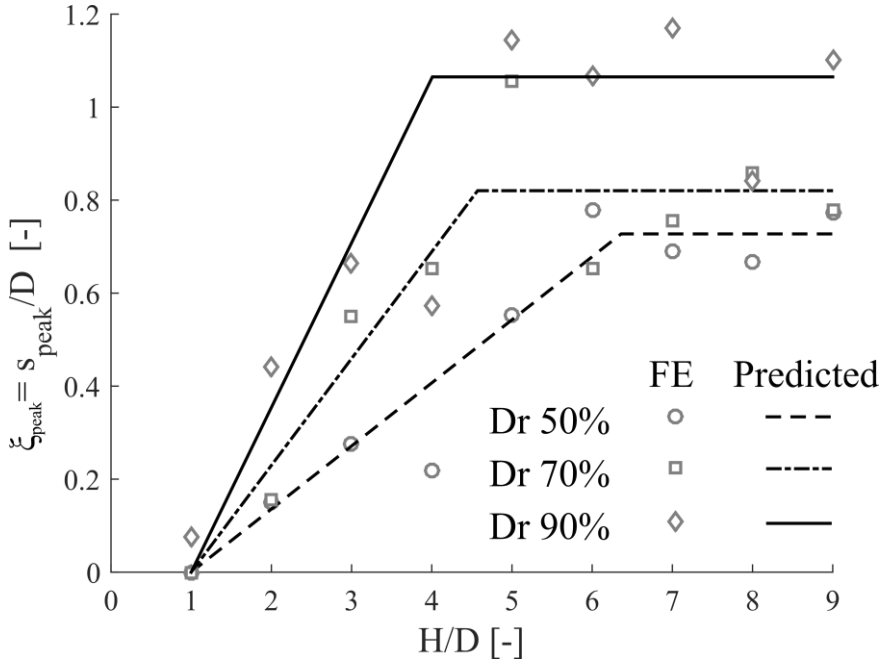

Figure 12 Normalised distance from the plate edge at which the maximum shear stress occurs as a function of density and relative embedment ratio, numerical results (markers), best-fit (line)

4.3. Generalisation to other sand properties

20

The previous analysis was carried out for a specific soil type (HST95 sand). The set of HS small parameters calibrated for this sand by Al-Defae et al. (2013) has been used as the reference in this study and thus it is necessary to demonstrate that the modified approach is applicable to other soil types. Capacity will principally be controlled by the soil's friction angle; however, the modifications to the shear stress distribution arise due to the stress field induced above the anchor plate as the soil compresses. It is therefore necessary to consider soils which may have different stiffness at similar strength.
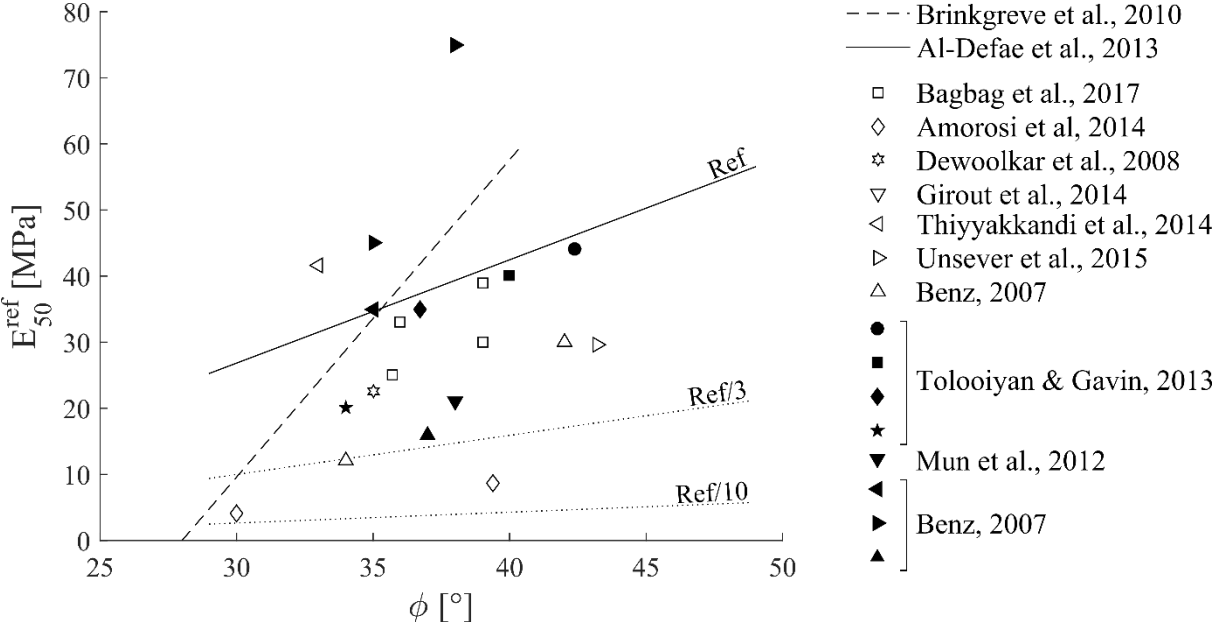
Figure 13 Relation between peak friction angle φ and reference secant stiffness E_{50}^{ref} calibrated for the HSsmall model and different types of soils (represented by different markers), open markers are for laboratory tests, closed markers are for field testing

Figure 13Figure 13 summarises parameters (strength φ and secant stiffness E_{ref}^{50}) of different soil materials/densities calibrated for the HS small model from the literature. The set of parameters used for this study is similar to several other soil materials, though it represents an upper bound of the results (i.e. HST95 sand is a soil of lower compressibility for its strength). Dividing the reference stiffness relationship (provided in Table 1Table 1) by a factor of 3 produces a lower bound to the majority of the indexed data. Dividing the stiffness by 10 encompasses also the results of Amorosi et al. (2014). Further numerical simulations were conducted with reduced stiffness parameters (E_{50}^{ref}, E_{oed}^{ref}, E_{ur}^{ref} and G_0^{ref}) with all other parameters being kept constant at the HST95 values.

The effect of lower soil stiffness on the bearing factor is depicted in Figure 14Figure 14. Simulations were run only for a reference case corresponding to a relative density of 90%. Results are presented as a relative numerical bearing factor variation with respect to the reference case $N_{\gamma,Eref}$, (Dr=90%). The whole range of relative embedment was not covered as the maximum displacement at depth became unacceptably large as the stiffness reduced. The anchor capacity is clearly reduced for all simulations due to a reduction in soil stiffness. However, there is no clear trend with the relative embedment. However, on average uplift capacities are approximately 10% lower if stiffness is divided by 3, incorporating almost all of the soils shown in Figure 13Figure 13. As a result, it can be concluded that the proposed

modification of the shear stress distribution is a good approximation over a wide range of soil conditions. In addition, underestimating the stiffness leads to a more conservative approach.
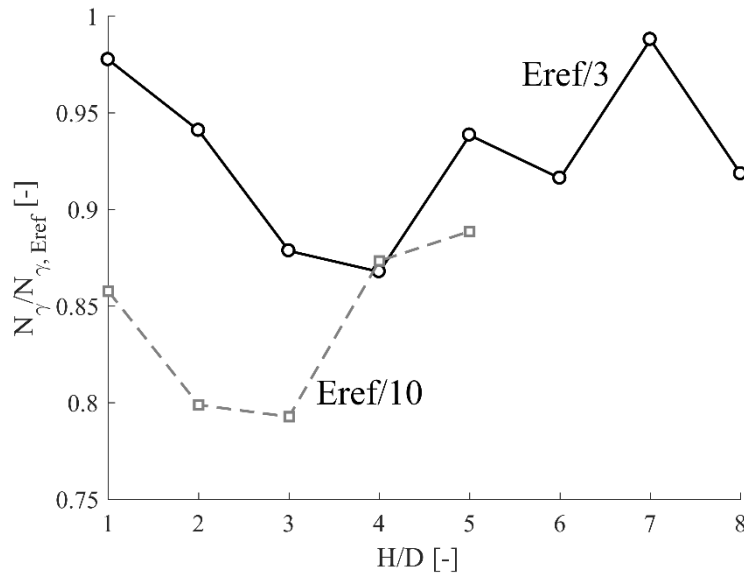

Figure 14 Variation of the bearing factor as a function of the stiffness (Eref) with respect to the reference case $N_{\gamma,Eref}$ (Dr=90%)

5. Conclusions

Experimental results and analytical criteria available in the literature to predict plate or single helix anchor capacity in sand are shown to provide very scattered results, depending on the study or body of work considered. In this work, a commercially available non-linear finite element code has been used to simulate uplift of large diameter plate anchors, embedded in sand at three different densities and up to large embedment depths. Numerical results were validated against available relatively large scale 1g, field and centrifuge tests.

Most existing analytical methods for estimating anchor capacity overpredict the results observed herein, particularly at large embedment depths. This results from the use of implicit empirical factors calibrated against small-scale 1g tests or the erroneous estimation of the failure mechanism inclination. However, the approach proposed by Giampa et al. (2017) assumes a correct inclination of the failure mechanism and predicts accurately results at shallow depths (H/D<4). Its predictions of the numerical results decrease as embedment depth increases.

This study shows that the soil compressibility plays a major role in the definition of the stress distribution along the failure mechanism. The common hypotheses of a failure surface between two rigid blocks and linear effective normal stress distributions are not consistent with the numerical results. Indeed, the vertical and subsequent horizontal soil deformation modify the stress distribution along the failure mechanism, namely it increases the normal and shear stresses. This effect directly dependent on the soil stiffness and reduces as the stiffness decreases.

A detailed analysis of the enhanced shear stress distributions observed numerically revealed that they could be described by a linearly increasing then exponentially decreasing

22

mathematical function, whose parameters (peak stress, distance of the peak from the anchor edge) can be identified as a function of the relative density of the soil and relative embedment ratio of the anchor. A transition can also be observed between deep embedments at which there is a significant increase of the normal and shear stress, and the shallow cases where this enhancement is very limited.

These findings should improve the upscaling of current plate and screw anchors design approaches for larger plates and screw piles, since strain required to mobilise failure should increase accordingly, modifying the stress field around the anchor.

6. Acknowledgements

7. Notation

A	Surface of the anchor
c	Effective cohesion
C	Parameter
D	Anchor diameter
H	Embedment depth of the anchor
H_0	Height of the truncated deep wedge
e_0	Initial void ratio
e_{min}	Minimum void ratio
e_{max}	Maximum void ratio
$E_{50}{}^{ref}$	Reference secant stiffness ($p_{ref} = 100$kPa)
$E_{oed}{}^{ref}$	Reference oedometric stiffness ($p_{ref} = 100$kPa)
$E_{UR}{}^{ref}$	Reference Unloading/reloading stiffness ($p_{ref} = 100$kPa)
F_y	Tensile load at failure
F_τ	Vertical resultant of the shear stress distribution along the failure mechanism
FE	Finite element
G_{0ref}	Reference low strain shear modulus ($p_{ref} = 100$kPa)
m	Material parameter
N_γ	Non-dimensional bearing factor
K_0	Coefficient of earth pressure at rest
K'_p	Earth pressure coefficient (Ghaly et al. 1991)
K_t	Coefficient of lateral earth pressure (Murray and Geddes 1987)
K_u	Coefficient of lateral earth pressure in uplift (Mitsch and Clemence 1985)
sK_u	Uplift coefficient (Meyerhof and Adams 1968)
N_{qu}	Uplift capacity factor (Mitsch and Clemence 1985)
s	Coordinate along the failure surface emanating from the edge of the anchor
z	Depth
α	Inclination to the vertical of the curved failure surface at the point where the resultant frictional force acts (Murray and Geddes 1987)
β	Inclination of the resultant of forces to the horizontal (Murray and Geddes 1987)

ϵ_v	Volumetric deformation
γ'	Buoyant unit weight
γ	Equivalent shear deformation
$\gamma_{0.7}$	Reference shear strain
γ_{tot}	Total unit weight
θ	Inclination of the conical failure mechanism to the vertical direction
κ	Decrease rate of the additional shear stress
ν_{UR}	Unloading/reloading Poison's ratio
ξ	Normalised distance from the plate edge (=s/D)
σ'_N	Normal effective stress (to the failure mechanism)
σ'_h	Horizontal effective stress
σ'_v	Vertical effective stress
τ	Shear stress
τ_G	Assumed shear stress obtained through Equation (88)
τ_{peak}	Peak shear stress along the failure mechanism
ϕ	Peak friction angle
ϕ_{mob}	Mobilised friction angle (Ghaly et al. 1991)
ψ	Peak dilatancy angle

8. References

Al-Baghdadi, T.A., Brown, M.J., Knappett, J.A., and Al-Defae, A.H. 2017a. Geotechnical engineering effects of vertical loading on lateral screw pile performance. Proceedings of the Institution of Civil Engineers: Geotechnical Engineering, **170**(3): 259–272. doi:10.1680/jgeen.16.00114.

Al-Baghdadi, T.A., Brown, M.J., Knappett, J.A., and Ishikura, R. 2015. Modelling of laterally loaded screw piles with large helical plates in sand. *In* 3rd International Symposium on Frontiers in Offshore Geotechnics. CRC Press/Balkema, Oslo, Norway. pp. 503–508.

Al-Baghdadi, T.A., Davidson, C., Brown, M.J., Knappett, J.A., Brennan, A., Augarde, C., Coombs, W., and Wang, L. 2017b. CPT based design procedure for installation torque prediction for screw piles installed in sand. 8th International Conference on Offshore Site Investigation & Geotechnics, (1).

Al-Defae, A.H., Caucis, K., and Knappett, J.A. 2013. Aftershocks and the whole-life seismic performance of granular slopes. Géotechnique, **63**(14): 1230–1244. doi:10.1680/geot.12.P.149.

Amorosi, A., Boldini, D., and Falcone, G. 2014. Numerical prediction of tunnel performance during centrifuge dynamic tests. Acta Geotechnica, **9**(4): 581–596. doi:10.1007/s11440-013-0295-7.

Anastasopoulos, I., Gazetas, G., Asce, M., Bransby, M.F., Davies, M.C.R., and Nahas, a El. 2007. Fault Rupture Propagation through Sand : Finite-Element. Journal of Geotechnical and Geoenvironmental Engineering, **133**(August): 943–958. doi:10.1061/(ASCE)1090-0241(2007)133:8(943).

Association', 'European Wind Energy. 2013. Deep water - The next step for offshore wind energy. *In* Deep water The next step for offshore wind energy.

Bagbag, A.A., Lehane, B.M., and Doherty, J.P. 2017. Predictions of footing and

24

pressuremeter response in sand using a hardening soil model. Proceedings of the Institution of Civil Engineers - Geotechnical Engineering, **170**(GE6): 1–14. doi:10.1680/jgeen.17.00040.

Baker, W.H., and Konder, R.L. 1966. Pullout load capacity of a circular earth anchor buried in sand. Highway Research Record, **108**.

Benz, T. 2007. Small-Strain Stiffness of Soils and its Numerical Consequences. PhD Thesis. University of Stuttgart.

Bradshaw, A., Giampa, J.R., Gerkus, H., Jalilvand, S., Fanning, J., Nanda, S., Gilbert, R., Gavin, K., and Sivakumar, V. 2016. Scaling considerations for 1-g model horizontal plate anchor tests in sand. Geotechnical Testing Journal, **39**(6): 1006–1014.

Brinkgreve, R., Engin, E., and Engin, H. 2000. Validation of empirical formulas to derive model parameters for sands. Numerical Methods in Geotechnical Engineering,: 137–142. doi:10.1201/b10551-25.

Byrne, B.W., and Houlsby, G.T. 2015. Helical piles: an innovative foundation design option for offshore wind turbines. Philosophical Transactions of the Royal Society A: Mathematical, Physical & Engineering Sciences, **373**(February): 1–11. doi:10.1098/rsta.2014.0081.

Caquot, A., and Kerisel, J. 1948. Tables de poussée et de butée. Gauthier-Villars, Paris.

Das, B.M., and Shukla, S.K. 2013. Earth anchors. J. Ross, Plantation, Florida.

Davidson, C., Al-Baghdadi, T., Brown, M., Brennan, A., Knappett, J., Augarde, C., W., C., Wang, L., Richards, D., Blake, A., and Ball, J. 2018. A modified CPT based installation torque prediction for large screw piles in sand. *In* Cone Penetration Testing. *Edited by M. Hicks, F. Pisanò, and J. Peuchen.* Delft, The Netherlands. doi:https://doi.org/10.1201/9780429505980.

Dewoolkar, M.M., Hwang, J., and Ko, H.Y. 2008. Physical and finite element modeling of lateral stability of offshore skirted gravity structures subjected to iceberg impact load. Ocean Engineering, **35**(16): 1615–1626. doi:10.1016/j.oceaneng.2008.08.005.

Dickin, E.A. 1988. Uplift behaviour of horizontal anchor plates in sand. Journal of Geotechnical and Geoenvironmental Engineering, **114**(11): 1300–1317.

Gaudin, C., Cassidy, M.J., O'Loughlin, C.D., Tian, Y., Wang, D., and Chow, S. 2017. Recent advances in anchor design for floating structures. *In* International Journal of Offshore and Polar Engineering. pp. 44–53. doi:10.17736/ijope.2017.jc673.

Gavin, K., Doherty, P., and Tolooiyan, A. 2014. Field investigation of the axial resistance of helical piles in dense sand. Canadian Geotechnical Journal, **51**(11): 1343–1354. doi:10.1139/cgj-2012-0463.

Ghaly, A., Hanna, A., and Hanna, M. 1991. Uplift behaviour of screw anchor in sand, I dry sand. Journal of Geotechnical Engineering, **117**(5): 773–793.

Giampa, J., Bradshaw, A., and Schneider, J. 2017. Influence of Dilation Angle on Drained Shallow Circular Anchor Uplift Capacity. International Journal of Geomechanics, **17**(2): 4016056. doi:10.1061/(ASCE)GM.1943-5622.0000725.

Giampa, J.R., Bradshaw, A., Gerkus, H., Gilbert, R.B., Gavin, K.G., and Sivakumar, V. 2018. The effect of shape on the pullout capacity of shallow plate anchors in sand.

Géotechnique,1-9. doi:10.1680/jgeot.17.P.269.

Girout, R., Blanc, M., Dias, D., and Thorel, L. 2014. Numerical analysis of a geosynthetic-reinforced piled load transfer platform - Validation on centrifuge test. Geotextiles and Geomembranes, **42**(5): 525–539. Elsevier Ltd. doi:10.1016/j.geotexmem.2014.07.012.

Hanna, A., Ayadat, T., and Sabry, M. 2007. Pullout resistance of single vertical shallow helical and plate anchors in sand. Geotechnical and Geological Engineering, **25**(5): 559–573. doi:10.1007/s10706-007-9129-4.

Ilamparuthi, K., Dickin, E.A., and Muthukrisnaiah, K. 2002. Experimental investigation of the uplift behaviour of circular plate anchors embedded in sand. Canadian Geotechnical Journal, **39**: 648–664. doi:10.1139/t02-005.

Ilamparuthi, K., and Muthukrishnaiah, K. 1999. Anchors in sand bed: Delineation of rupture surface. Ocean Engineering, **26**(12): 1249–1273. doi:10.1016/S0029-8018(98)00034-1.

Jaky, J. 1944. The coefficient of earth pressure at rest. Journal of the Society of Hungarian Architects and Engineers, **78**(5): 355–358.

Jeffrey, J., Brown, M.J., Knappett, J.A., Ball, J.D., and Caucis, K. 2016. CHD pile performance : part I – physical modelling. Proceedings of the ICE - Geotechnical Engineering, **169**(5): 436–454. doi:10.1680/jgeen.15.00132.

Knappett, J.A., Caucis, K., Brown, M.J., Jeffrey, J.R., and Ball, J.D. 2016. CHD pile performance: part II – numerical modelling. Proceedings of the Institution of Civil Engineers - Geotechnical Engineering, **169**(5): 436–454. doi:10.1680/jgeen.15.00132.

Knappett, J.A., and Craig, F. 2012. Craig's soil mechanics, 8th Edition. CRC Press.

Lauder, K. 2010. The performance of pipeline ploughs. PhD Thesis. University of Dundee.

Liu, J.Y., Liu, M.L., and Zhu, Z.D. 2012. Sand Deformation around an Uplift Plate Anchor. Journal of Geotechnical and Geoenvironmental Engineering, **138**(6): 728–737. doi:Doi 10.1061/(Asce)Gt.1943-5606.0000633.

Merifield, R.., Sloan, S.W., and Lyamin, A.V. 2003. Three Dimensional Lower Bound Solutions for the Stability of Plate Anchors in Sand. Technical Report.

Merifield, R.S., and Sloan, S.W. 2006. The ultimate pullout capacity of anchors in frictional soils. Canadian Geotechnical Journal, **43**(8): 852–868. doi:10.1139/t06-052.

Meyerhof, G.G., and Adams, J.I. 1968. The ultimate uplift capacity of foundations. Canadian Geotechnical Journal, **5**(4).

Mitsch, M.P., and Clemence, S.. 1985. The uplift capacity of helix anchors in sand. *In* Uplift behavior of anchor foundations in soil, ASCE. pp. 26–47.

Mun, B., Kim, T., Moon, T., and Oh, J. 2012. SCM wall in sand: Numerical simulation and design implications. Engineering Geology, **151**: 15–23. Elsevier B.V. doi:10.1016/j.enggeo.2012.09.003.

Murray, E.F., and Geddes, J.D. 1987. Uplift of anchor plates in sand. ASCE Journal of geotechnical engineering, **113**(3): 202–215. doi:10.1016/0148-9062(87)91096-5.

Newgard, J.T., Schneider, J. a., and Thompson, D.J. 2015. Cyclic response of shallow helical anchors in a medium dense sand. *In* 3rd International Symposium on Frontiers in

Offshore Geotechnics. CRC Press/Balkema, Oslo, Norway. pp. 503–508.~~Frontiers in Offshore Geotechnics III, 1~~pp: 913–918. doi:10.1201/b18442-131.

O'Loughlin, C.D., Blake, A.P., Richardson, M.D., Randolph, M.F., and Gaudin, C. 2014. Installation and capacity of dynamically embedded plate anchors as assessed through centrifuge tests. Ocean Engineering, **88**: 204–213. ~~Elsevier.~~ doi:10.1016/j.oceaneng.2014.06.020.

Perez, Z.A., Schiavon, J.A., Tsuha, C.H.C., Dias, D., and Thorel, L. 2017. Numerical and experimental study on the influence of installation effects on the behaviour of helical anchors in very dense sand. Canadian Geotechnical Journal, 55(8): 1067-1080, doi:10.1139/cgj-2017-0137.

Perko, H.A. 2009. Helical Piles: A Practical Guide to Design and Installation. *~~In 1~~*First Edition. John Wiley & Sons. doi:10.1002/9780470549063.

PLAXIS. 2017a. PLAXIS 2D Reference Manual. Delft, The Netherlands.

PLAXIS. 2017b. PLAXIS Material Models Manual. Delft, The Netherlands.

Prandtl, L. 1921. Hauptaufsätze: Über die eindringungsfestigkeit (härte) plastischer baustoffe und die festigkeit von schneiden. ZAMM-Journal of Applied Mathematics and Mechanics/Zeitschrift für Angewandte Mathematik und Mechanik, **1**(1): 15–20.

Randolph, M.F. 2003. Science and empiricism in pile foundation design. Géotechnique, **53**(10): 847–875. doi:10.1680/geot.2003.53.10.847.

Randolph, M.F., Gaudin, C., Gourvenec, S.M., White, D.J., Boylan, N., and Cassidy, M.J. 2011. Recent advances in offshore geotechnics for deep water oil and gas developments. Ocean Engineering, **38**(7): 818–834. Elsevier. doi:10.1016/j.oceaneng.2010.10.021.

Rasulo, M.P., Schneider, J.A., Newgard, J.T., and Aubeny, C.P. 2017. Transition depths for deep circular anchors in saturated sand. *In* Offshore Site Investigation Geotechnics 8th International Conference Proceeding. pp. 987–994.

Saeedy, H. 1987. Stability of circular vertical earth anchors. Canadian Geotechnical Journal, **24**: 452–456.

Schanz, T., Vermeer, A., and Bonnier, P. 1999. The hardening soil model: formulation and verification. Beyond 2000 Comput. Geotech. 10 years PLAXIS~~Beyond 2000 Comput. Geotech. 10 years PLAXIS Int. Proc. Int. Symp. beyond 2000 Comput. Geotech~~. Amsterdam Netherlands ~~1820~~March 1999,: 281-296.

Schiavon, J.A., Tsuha, C.H.C., and Thorel, L. 2016. Scale effect in centrifuge tests of helical anchors in sand. International Journal of Physical Modelling in Geotechnics, **16**(4): 185–196.

Schneider, J.A., Giampa, J.R., Bradshaw, A., and Newgard, J.T. 2016. Calibrating CPT relative density and strength correlations for a laboratory fine sand. *In 5*[th] International Conference on Geotechnical and Geophysical Site Characterisation, ~~1(32):~~Australia. pp 449–454.

Sutherland, H.B. 1965. Model Studies for Shaft Raising through Cohesionless Soils. *In* Proceedings of the 6th International Conference on Soil Mechanics and Foundation Engineering, Montréal. Montreal, Canada. pp. 410–413.

Tappenden, K.M. 2007. Predicting the axial capacity of screw piles installed in Canadian

soils. Master Thesis. University of Alberta.

Thiyyakkandi, S., McVay, M., Bloomquist, D., and Lai, P. 2014. Experimental study, numerical modeling of and axial prediction approach to base grouted drilled shafts in cohesionless soils. Acta Geotechnica, **9**(3): 439–454. doi:10.1007/s11440-013-0246-3.

Tolooiyan, A., and Gavin, K. 2013. The base resistance of non-displacement piles in sand . Part II : finite-element analyses. Geotechnical Engineering: Proceedings of the Institution of Civil Engineers, **166**: 549–560. doi:10.1680/geng.11.00101.

Tucker, K.. 1987. Uplift capacity of drilled shafts and driven piles in granular materials. *In* Foundations for transmission line towers. pp. 142–159.

Unsever, Y.S., Matsumoto, T., and Özkan, M.Y. 2015. Numerical analyses of load tests on model foundations in dry sand. Computers and Geotechnics, **63**: 255–266. Elsevier Ltd. doi:10.1016/j.compgeo.2014.10.005.

Vesic, A. 1971. Breakout resistance of objects embedded in ocean bottom. Journal of the Soil Mechanics and Foundations Division. Proceedings of the American Society of Civil Engineers, **97**(SM9): 1183–1205.

Vesic, A., Wilson, W.E., and Clough, G.. 1965. Theoretical studies of cratering mechanisms affecting the stability of cratered slopes, Phase II. Atlanta. Technical Report No 3-699, Georgia Institute of Technology, Atlanta, USA.

Vesic, N. 1969. Breakout resistance of objects embedded in ocean bottom. Technical Report No CR.69.031. Duke University

White, D.J., Cheuk, C.Y., and Bolton, M.D. 2008. The uplift resistance of pipes and plate anchors buried in sand. Géotechnique, **58**(10): 771–779. doi:10.1680/geot.2008.3692.

"Wind Europe Business Intelligence."Wind Europe 2018. Offshore wind in Europe. *In Offshore Wind in Europe*: key trends and statistics 2017. Technical Report, Brussels, Belgium doi:10.1016/S1471-0846(02)80021-X.

Figure 1

Figure 1

Sand properties:

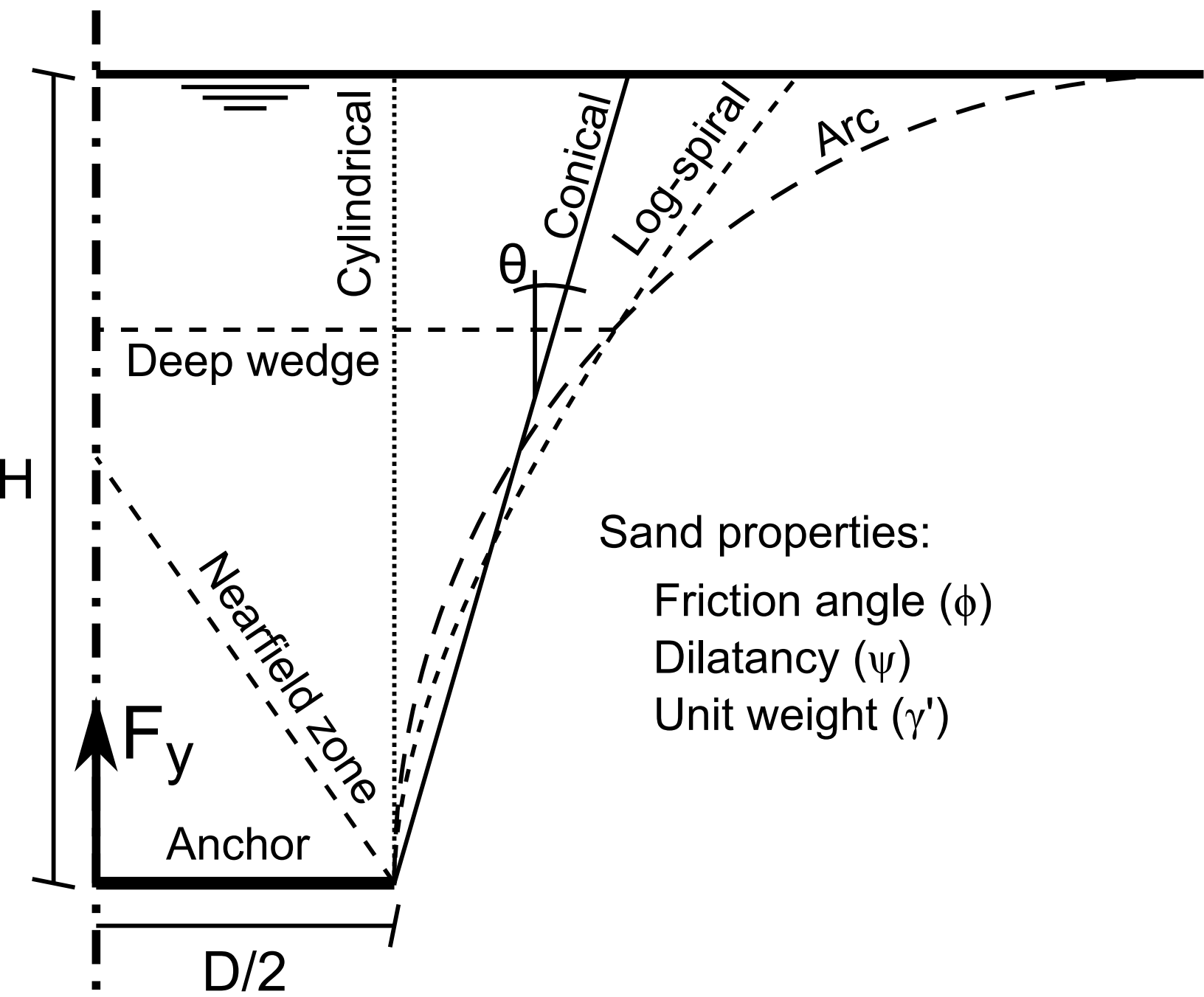Friction angle (ϕ)
Dilatancy (ψ)
Unit weight (γ')

Figure 2

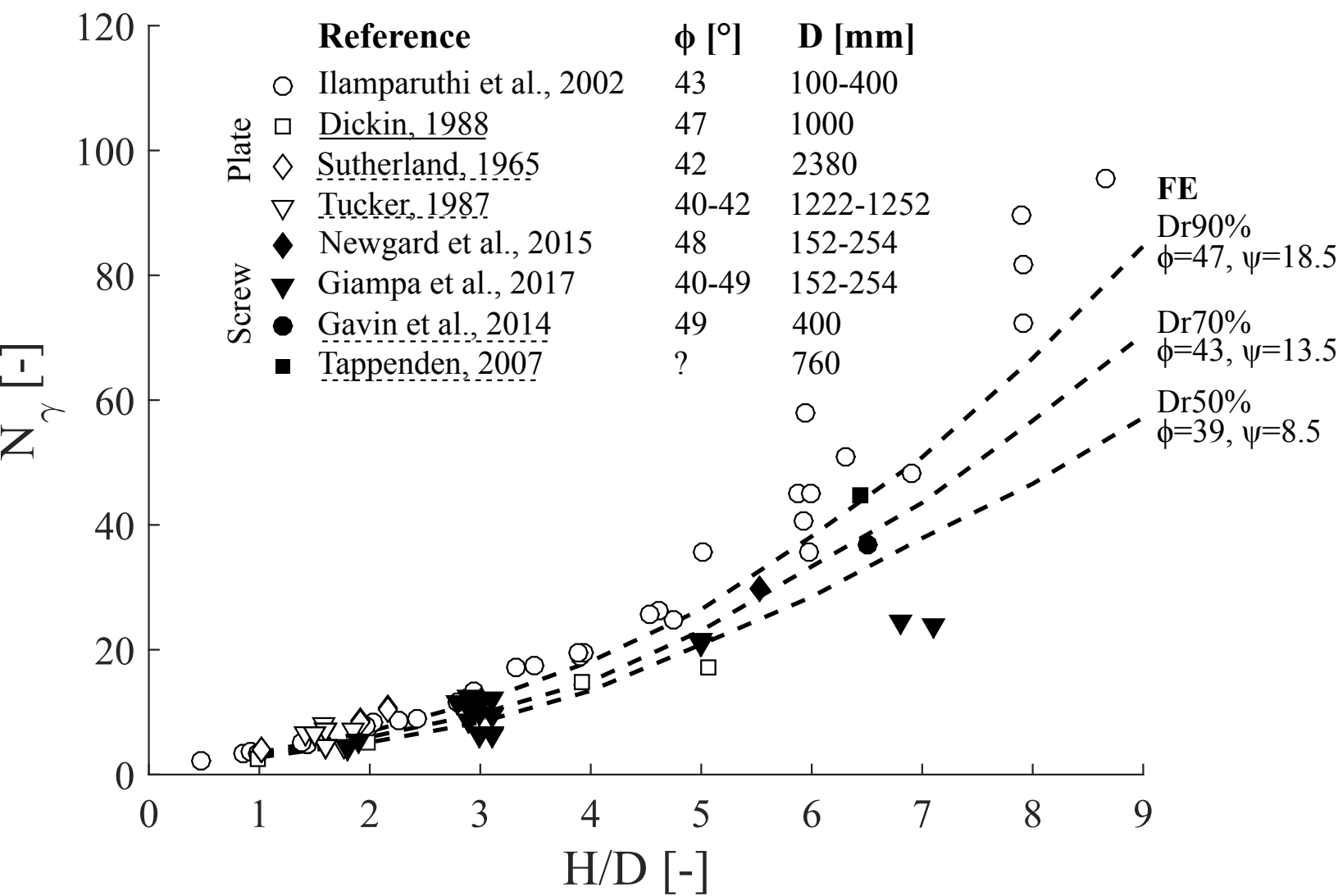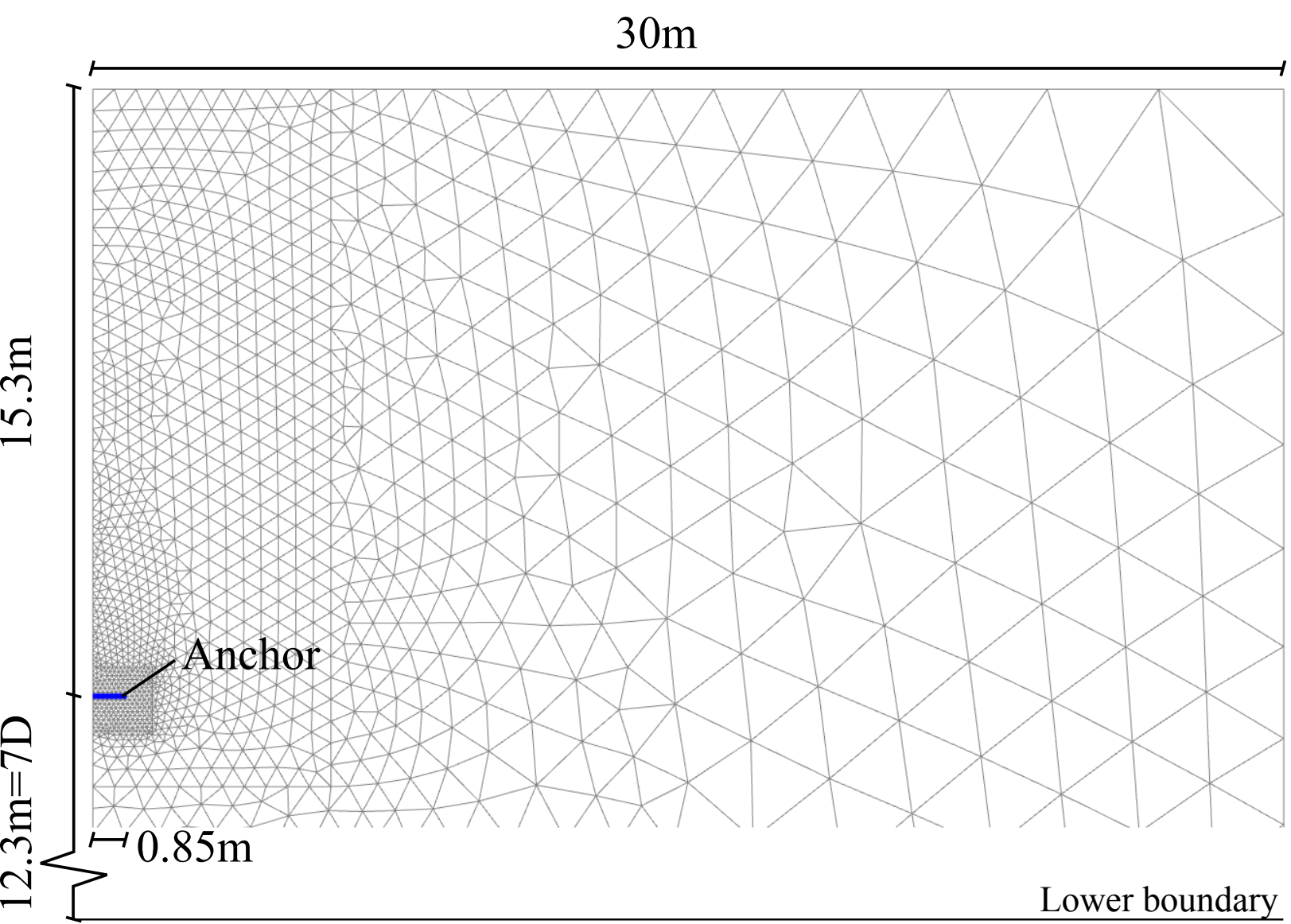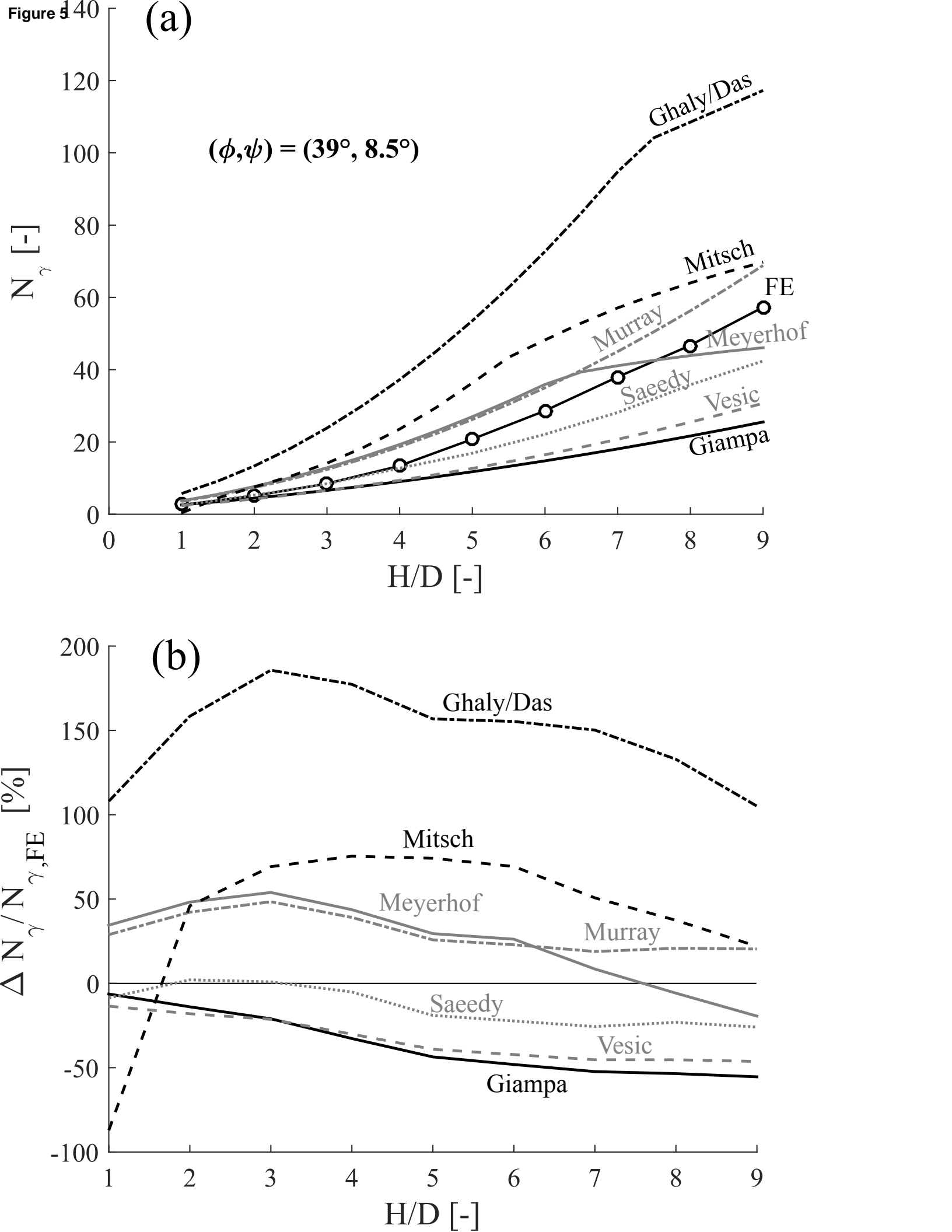**Figure 3**
[Click here to download high resolution image](#)

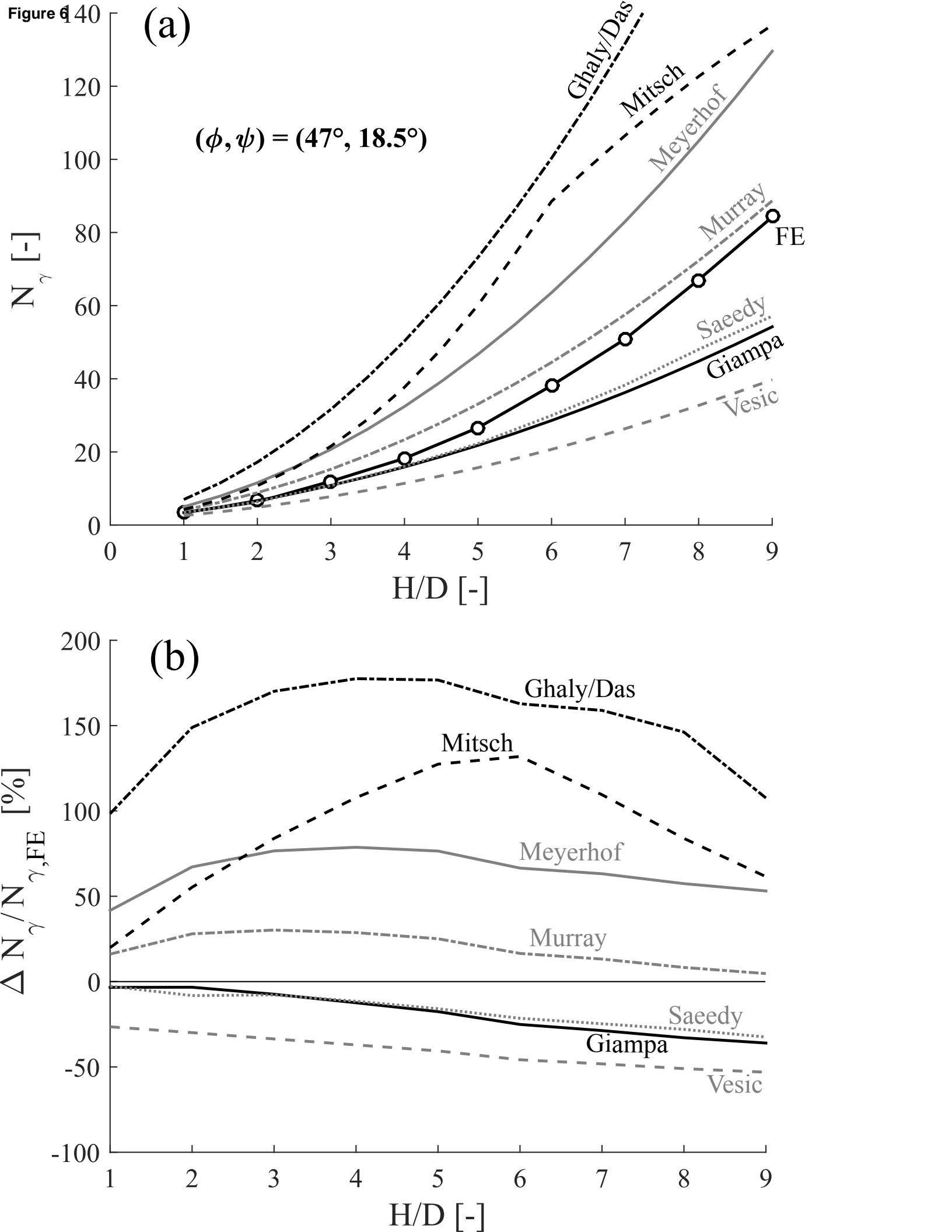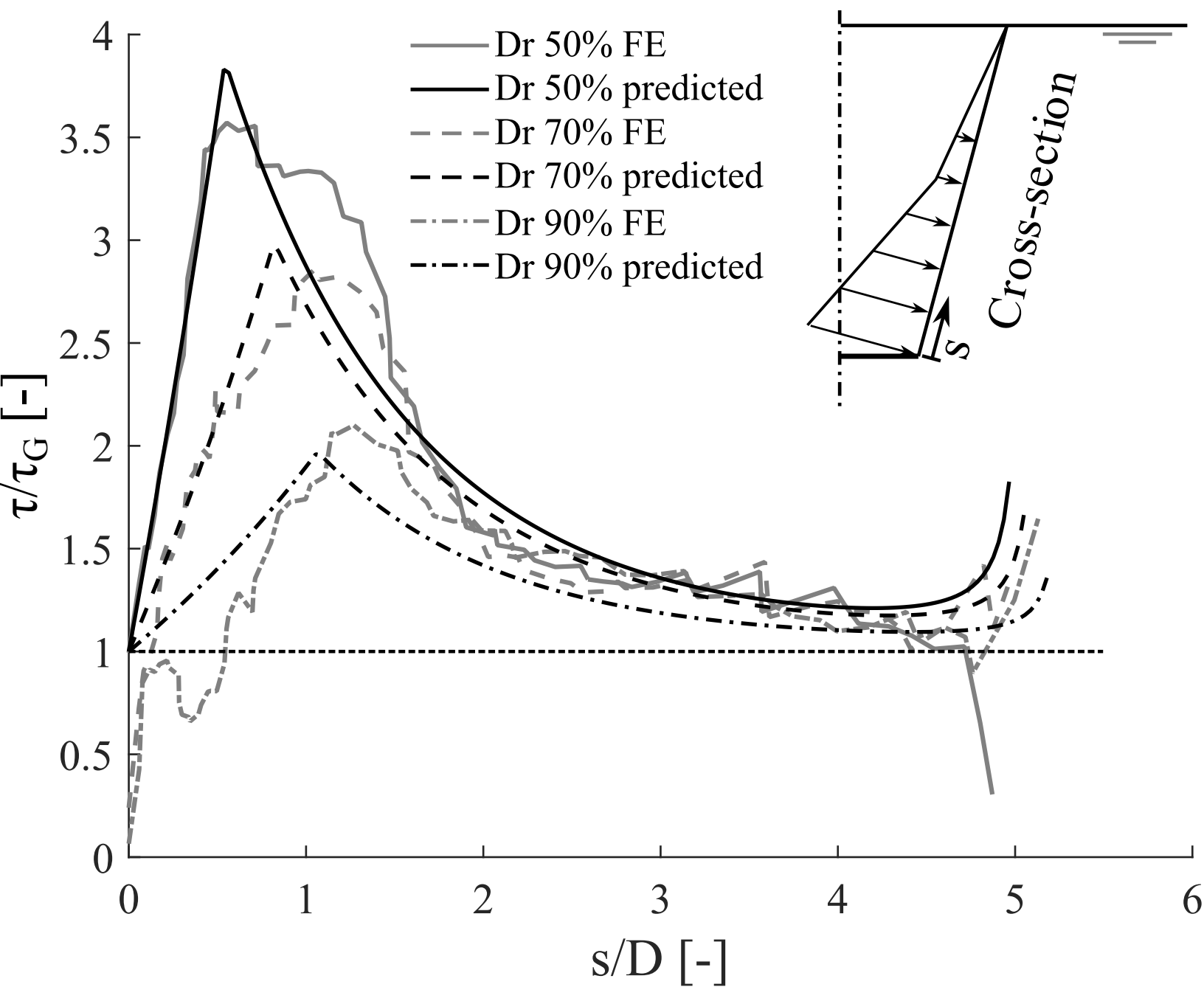(a) Dr = 50%
$\phi = 39°$
$\psi = 8.5°$

(b) Dr = 70%
$\phi = 43°$
$\psi = 13.5°$

(c) Dr = 90%
$\phi = 47°$
$\psi = 18.5°$

Figure 4

30m

15.3m

Anchor

12.3m=7D

0.85m

Lower boundary

Figure 5

(a)

$(\phi,\psi) = (39°, 8.5°)$

Ghaly/Das

Mitsch

FE

Murray

Meyerhof

Saeedy

Vesic

Giampa

(b)

Ghaly/Das

Mitsch

Meyerhof

Murray

Saeedy

Vesic

Giampa

Figure 6

(a)

$(\phi, \psi) = (47°, 18.5°)$

Ghaly/Das

Mitsch

Meyerhof

Murray

FE

Saeedy

Giampa

Vesic

N_γ [-]

H/D [-]

(b)

Ghaly/Das

Mitsch

Meyerhof

Murray

Saeedy

Giampa

Vesic

$\Delta N_\gamma / N_{\gamma,FE}$ [%]

H/D [-]

Figure 7
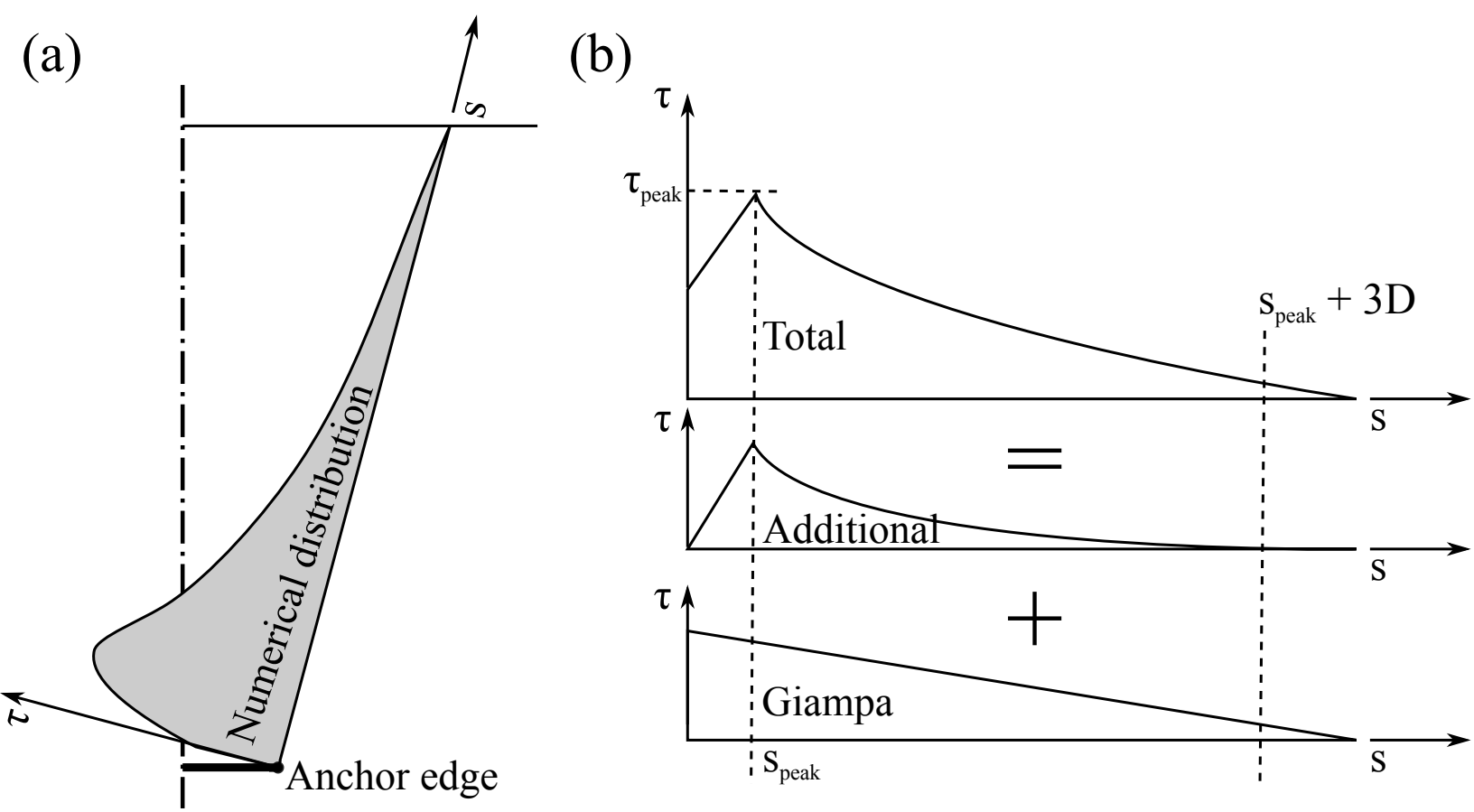
Figure 8
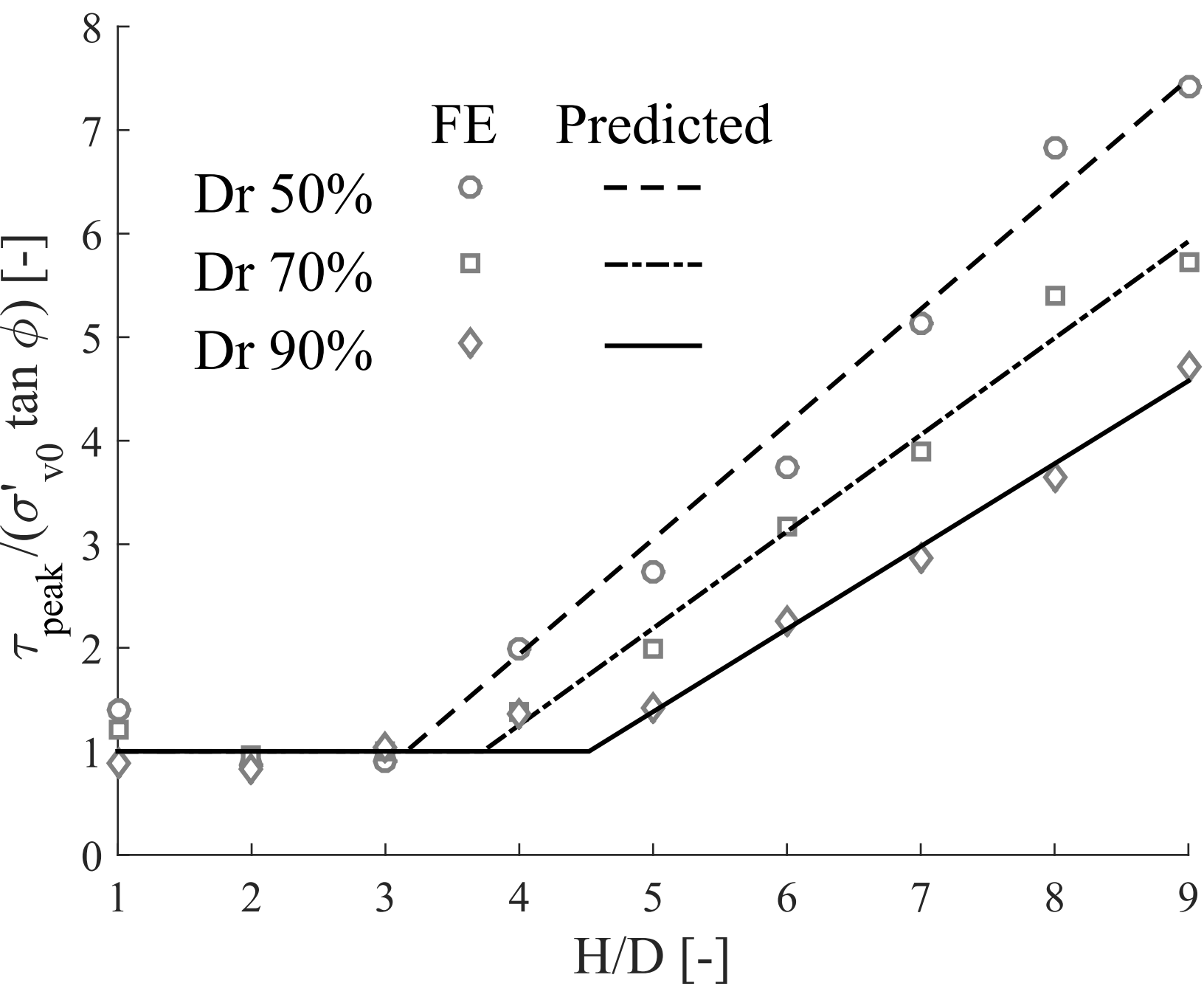
Figure 10

Figure 11

Figure 12

Figure 13

Figure 14